Draft version April 22, 2025
Typeset using LaTeX twocolumn style in AASTeX631

arXiv:2504.13997v1 [astro-ph.EP] 18 Apr 2025

A Revised Density Estimate for the Largest Known Exoplanet, HAT-P-67 b

Gavin Wang,[1] William O. Balmer,[1,2,*] Laurent Pueyo,[2] Daniel Thorngren,[1] Stephen P. Schmidt,[1,†] Le-Chris Wang,[1] Kevin C. Schlaufman,[1] Guðmundur Stefánsson,[3] Zafar Rustamkulov,[4] and David K. Sing[1,4]

[1] William H. Miller III Department of Physics & Astronomy, Johns Hopkins University, 3400 N. Charles Street, Baltimore, MD, USA
[2] Space Telescope Science Institute, 3700 San Martin Dr, Baltimore, MD, USA
[3] Anton Pannekoek Institute for Astronomy, University of Amsterdam, Science Park 904, 1098 XH Amsterdam, The Netherlands
[4] Morton K. Blaustein Department of Earth & Planetary Sciences, Johns Hopkins University, Baltimore, MD, USA

(Received 2025 January 28; Revised 2025 March 31; Accepted 2025 April 17)

ABSTRACT

Low-density ($\rho < 0.1$ g cm^{-3}) hot Saturns are expected to quickly (< 100 Myr) lose their atmospheres due to stellar irradiation, explaining their rarity. HAT-P-67 b seems to be an exception, with $\rho < 0.09$ g cm^{-3} and maintaining its atmosphere to well after 1 Gyr. We present a photometric and spectroscopic follow-up of HAT-P-67 b to determine how it avoided mass loss. HAT-P-67 b orbits a $V = 10.1$ evolved F-type star in a 4.81 day orbit. We present new radial velocity observations of the system from the NEID spectrograph on the WIYN 3.5m Telescope from a follow-up campaign robust to stellar activity. We characterize the activity using photometry and activity indicators, revealing a stellar rotation period (5.40 ± 0.09 d) near HAT-P-67 b's orbital period. We mitigate the stellar activity using a constrained quasi-periodic Gaussian process through a joint fit of archival ground-based photometry, TESS photometry, and our NEID observations, obtaining a planetary mass of $M_p = 0.45 \pm 0.15$ M$_\mathrm{J}$. Combined with a radius measurement of $R_p = 2.140 \pm 0.025$ R$_\mathrm{J}$, this yields a density of $\rho_p = 0.061^{+0.020}_{-0.021}$ g cm^{-3}, making HAT-P-67 b the second lowest-density hot giant known to date. We find the recent evolution of the host star caused mass loss for HAT-P-67 b to only recently occur. The planet will be tidally disrupted in $\sim 100 - 250$ Myr, shortly after losing its atmosphere. With rapid atmospheric mass loss, a large, helium leading tail, and upcoming observations with the Hubble Space Telescope, HAT-P-67 b is an exceptional target for future studies, for which an updated mass measurement provides important context.

Keywords: Exoplanet Astronomy (486) — Exoplanet tides (497) — Exoplanets (498) — Extrasolar gaseous giant planets (509) — Radial velocity (1332) — Stellar activity (1580) — Transit photometry (1709)

1. INTRODUCTION

The most common method of determining exoplanet masses is the radial velocity (RV) method, which measures the Doppler shifts induced on the host star's spectrum by the motion of the star-planet system about its common barycenter (e.g., Struve 1952; Lovis & Fischer 2010; Perryman 2018). Given the mass of the host and the amplitude of the Doppler signal, a planetary mass, depending on the inclination of the planet's orbit with respect to the line of sight, can be inferred. Despite an order of magnitude improvement in precision (e.g., Mahadevan et al. 2012; Schwab et al. 2016; Gibson et al. 2016; Pepe et al. 2021) since the first RV detection of an exoplanet (Mayor & Queloz 1995), the impact of stellar activity on the detectable stellar semi-amplitude has confounded the detection and characterization of planets with this technique (Suárez Mascareño et al. 2022; Blunt et al. 2023). Variations in the star's photosphere, mag-

Corresponding author: Gavin Wang
gwang59@jhu.edu

* Johns Hopkins University George Owen Fellow
† NSF Graduate Research Fellow

netic field, or circumstellar environment impart stochastic noise onto the spectrum of the host star, which can influence Doppler measurements (Saar & Donahue 1997; Robertson et al. 2015; Gupta et al. 2021; Tran & Bowler 2024). Disentangling and revealing the planetary signal from this stochastic noise requires detailed analysis of the data (e.g., Nava et al. 2019; Gan et al. 2020; Blunt et al. 2023).

As of January 2025, HAT-P-67 b is reported to be the second lowest-density transiting hot giant planet known by the NASA Exoplanet Archive,[1] behind WASP-193b (Barkaoui et al. 2024). With a radius of 2.1 R_J and a mass of only $0.34^{+0.25}_{-0.19}$ M_J (Zhou et al. 2017, hereafter Z17), HAT-P-67 b exists in an exceptional density regime of $\rho < 0.1$ g cm^{-3}. Recent atmospheric transmission studies by Bello-Arufe et al. (2023), Gully-Santiago et al. (2024), and Sicilia et al. (2024) have found evidence for a large, leading helium tail and a high mass loss rate, which indicate that the planet is evaporating due to the incident radiation from its host star. Given the planet's equilibrium temperature (1900 K; Z17), low density, and large scale height ($\sim$ 800 km), it is an exceptional candidate for transmission spectroscopy to probe limb-to-limb variations, atmospheric dynamics, cloud condensation, and more. A mass uncertainty of 75%, however, inhibits an accurate determination of the planet's atmospheric properties (Batalha et al. 2019).

Thorngren et al. (2023) demonstrates, however, that low-density hot Saturns are expected to quickly lose their outer gas layers through runaway mass loss driven by extreme ultraviolet (XUV) irradiation from the host star. This runaway effect reproduces the observed trends in mass-radius space for the current population of hot-Saturns, namely the paucity of gas giants with densities below 0.1 g cm^{-3}. The mass measurement of HAT-P-67 b from Z17 places the planet significantly outside this regime, such that it is expected to have lost all of its envelope by its current age.

This observation has two possible explanations. First, there has been a recent change in the system, either inward migration or the evolution of the star into the subgiant branch (such that the XUV flux from the host star has not had sufficient time to remove its atmosphere). Second, stellar variability could have misled the mass measurement, and the planet is instead more massive. The host star HAT-P-67 has a high $v \sin i_*$ of $\sim$ 30 km/s (Z17) and has had signs of activity yielding large changes in radial velocity (Sicilia et al. 2024).

In this paper, we differentiate between these two hypotheses through a detailed investigation of the star's radial velocities. We confirm a Saturn-like mass for the planet at higher statistical significance with additional radial velocity observations from the NEID spectrograph on the WIYN 3.5m Telescope at Kitt Peak National Observatory (KPNO),[2] preserving a < 0.1 g cm^{-3} density. This provides evidence in favor of a recent change in the system's state, the first hypothesis presented above.

The remainder of this paper is organized as follows. §2 describes our photometric and spectroscopic data, as well as the modeling procedures we implement for each dataset. In §3 we perform a joint modeling of all data and present updated planetary parameters for HAT-P-67 b, in particular a revised mass of $M_p = 0.45 \pm 0.15$ M_J, radius of $R_p = 2.140 \pm 0.025$ R_J, and a density of $\rho_p = 0.061^{+0.020}_{-0.021}$ g cm^{-3}. §4 discusses the theoretical implications of our results and the fate of the planet. We end with a conclusion in §5.

2. DATA

2.1. *NEID Radial Velocities*

NEID (Schwab et al. 2016) is a high-resolution ($R = 100,000$) temperature-stabilized (Stefansson et al. 2016; Robertson et al. 2019) spectrograph on the 3.5-meter WIYN telescope at Kitt Peak National Observatory. NEID covers a broad wavelength range from 380 to 930 nm. At the time of our observations (2022 to 2023), HAT-P-67 b had already been discovered with a precise ephemeris, but had an uncertain mass measurement of $0.34^{+0.25}_{-0.19}$ M_J (Z17). As the goal of our RV follow-up was to determine the mass with higher precision, we preferentially targeted the RV quadrature phases (-0.25 and $+0.25$, with phase 0 being when the planet transits), when the RV amplitude would be expected to be greatest. Our observing strategy was to take 3 consecutive exposures of 600 seconds each night the planet was at or near quadrature. This strategy helps to average over RV variations driven by high frequency stellar oscillations. Given the estimated RV jitter, $\sigma_{\rm jit} = 59$ m/s (Z17, their Table 6), after the three observations are added in quadrature, this strategy was intended to achieve an uncertainty of $\sim$ 64 m/s. We note that the RV jitter is of comparable amplitude to the planetary signal, which is larger than for solar-type stars (e.g., jitter-to-planet amplitude ratio of $\sim$ 0.1 for 51 Peg; Mayor & Queloz 1995)

[1] https://exoplanetarchive.ipac.caltech.edu/cgi-bin/TblView/nph-tblView?app=ExoTbls&config=PS

[2] The WIYN Observatory is a joint facility of the NSF's National Optical-Infrared Astronomy Research Laboratory, Indiana University, the University of Wisconsin-Madison, Pennsylvania State University, Purdue University and Princeton University.

but not the largest (e.g., ratio of $5-8$ for V1298 Tau; Suárez Mascareño et al. 2022).

Observations of HAT-P-67 b were initially planned to be taken from May through July of 2022 but were cut short due to the Contreras Fire on 2022 June 12. Only 27 spectra (3 spectra per night for 9 nights) were taken between 2022 May 24 and 2022 June 12 before the site had to be shut down. Due to the target's visibility from the site (February through July), observations resumed the following year and an additional 48 spectra were taken from 2023 February 27 to 2023 July 5. In total, this amounts to 75 spectra, with the majority being taken after the fire. During the fire, the instrument was put through a vacuum cycle, resulting in an RV offset e.g., due to subtle changes in the instrument point spread function. Thus, in our analysis, we treat the RV data before and after the fire as separate independent instruments, assigning them independent RV offsets and jitter values.

2.1.1. *SERVAL Pipeline*

The NEID spectra were extracted using the NEID Data Reduction Pipeline (DRP)[3] and retrieved from the NEID archive.[4] To extract RVs, we used a modified version of the Spectrum Radial Velocity Analyzer (SERVAL; Zechmeister et al. 2018) pipeline following Stefànsson et al. (2022), which uses as-observed spectral templates to extract RVs from the data. This resulted in median RV uncertainties of 26 m/s in the unbinned data. For comparison, the RV uncertainty reported by the NEID DRP, which are based on cross-correlation functions, were 124 m/s and showed large RV variations of > 500 m/s, oftentimes over a length of just a few days, and such variations were not seen in the HIRES dataset. We believe these excursions in the DRP RVs are likely due to the broad CCFs. Instead, the SERVAL pipeline self-consistently accounts for the RV uncertainties in the broadened as-observed templates. Given that our data spanned the instrument vacuum cycle due to the Contreras fire, we experimented extracting RVs from templates that spanned the whole data stream along with independently extracting RVs from templates generated using data before and after the fire. In both cases the RVs were equivalent. As such, we elected to use the extraction that generated a template using all of the data.

2.2. *HIRES Radial Velocities*

[3] https://neid.ipac.caltech.edu/docs/NEID-DRP/

[4] https://neid.ipac.caltech.edu/search.php

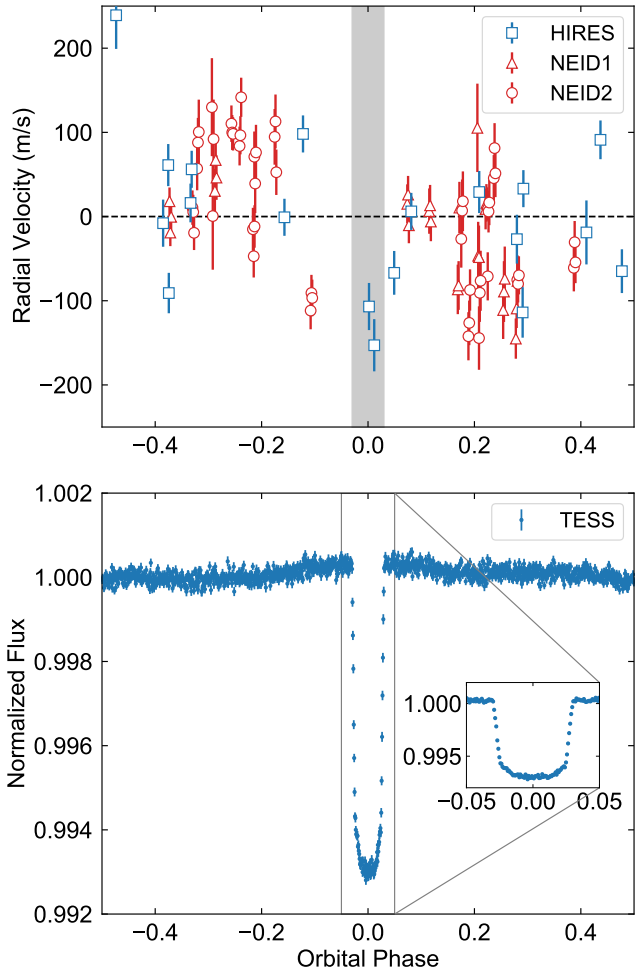

Figure 1. Top: Zero-pointed and phased RVs including both the HIRES (blue squares) and NEID (red triangles and circles) data. The two HIRES datapoints which fall in the shaded region are affected by the RM effect and thus excluded. The two datasets exhibit similar variational amplitude consistent with the upper bound from Z17. **Bottom:** Phase-folded light curve from TESS with bins of 100 points, demonstrating the existence of HAT-P-67 b.

The High Resolution Echelle Spectrometer (HIRES; Vogt et al. 1994) is a high-resolution ($R = 55,000$) spectrometer on the 10 m Keck Observatory at the Mauna Kea Observatories. High-precision radial velocities from HIRES of HAT-P-67 were published by Z17 (see their Table 3). A total of 19 spectra were taken between July 2009 and March 2012. Z17 did not detect an obvious orbit for the planet, and thus provided an upper constraint on the RV semi-amplitude based on the data. We are able to replicate the results in that work through a `juliet` (Espinoza et al. 2019a) fit of all 19 measurements using wide priors and without the use of a Gaussian process. For our joint analyses, we discard the two data points which are collected at phase 0.002 and 0.012,

Table 1. Radial velocity data from NEID. The full table is available online in machine-readable form.

BJD_{TDB}	RV (m/s)	σ_{RV} (m/s)	Instrument[a]
2459723.87646187	78.555	52.491	NEID1
2459723.88356815	−73.380	40.301	NEID1
2459723.89063798	−75.033	37.503	NEID1
2459725.90326585	−8.646	16.371	NEID1
2459725.91048804	−45.845	16.097	NEID1

[a] NEID1 refers to data collected before the June 2022 Contreras Fire; NEID2 refers to data collected after

which are when the planet is transiting. Due to the rapid spin of the host star, the Rossiter-McLaughlin (RM) effect is non-negligible (Rossiter 1924; McLaughlin 1924), and indeed Sicilia et al. (2024) finds a 200 m/s semi-amplitude RM effect for HAT-P-67 b. All radial velocity measurements phased to the planet period are plotted in Figure 1.

Due to the low mass of the companion, the sinusoidal signal in the radial velocities is not immediately obvious, although the average radial velocity for phases > 0 and < 0 are noticeably different. To briefly confirm the information content of the observations, we fit all of the radial velocity data while keeping the period fixed but the phase (t_0) free, and we find we are able to reproduce a phase consistent with that from Z17.

2.3. *HATNet Photometry*

The Hungarian-made Automated Telescope Network (HATNet; Bakos et al. 2004) monitored HAT-P-67 over a period of 7 months each in 2005 and 2008. This light curve data is publicly available in three forms: raw, External Parameter Decorrelation (EPD), and Trend Filtering Algorithm (TFA) magnitudes. Upon converting these magnitudes to relative fluxes and fitting with a single-planet transit model at HAT-P-67 b's ephemeris, we find that the TFA magnitudes are able to provide the best constraints on the transit parameters for HAT-P-67 b and thus we use these data for all of our following analyses. The corresponding log model evidence for each form of data is presented in Table 2.

We note that the data has been collected through two filters: the I filter for the 2005 data and the R_C filter for the 2008 data. Different photometric bandpasses yield different limb darkening solutions and instrumental systematics, and thus the common practice is to treat such data collected using the same instrument but different filters as two independent instruments. To test this hypothesis, we fit our data using `juliet` with uniform priors on the transit hyperparameters. We repeat the fit twice, once modeling the entire HATNet dataset with the same parameters and a second time stratifying the data by wavelength (i.e., defining separate median flux and jitter values for each filter). Indeed, we find that the stratification results in a higher log-evidence with $\Delta \ln \mathcal{Z} = 137.2$ (34181.3 versus 34044.1; see Table 2). In addition, since there are two photometric bandpasses, this results in an increase of only two parameters and does not significantly increase computation time for our final fits in §3.

Table 2. Log-evidences, a measure of how well the model fits the data, with better agreement corresponding to higher values, for fits to various combinations of photometric datasets.

Dataset	$\ln \mathcal{Z}$	Notes [✓?]
HATNet Raw	30376.551	Single instrument
HATNet EPD	32070.551	Single instrument
HATNet TFA	34044.117	Single instrument
HATNet TFA	34181.261	Stratified by band [✓]
KeplerCam	18534.661	Stratified by night
KeplerCam	18288.924	Single instrument [✓]
TESS	442731.659	Single instrument [✓]
TESS	442723.130	Stratified by sector

NOTE—Configurations used in final modeling denoted by ✓

2.4. *KeplerCam Follow-Up Photometry*

We made use of ground-based follow-up light curves from Z17 which were published alongside the discovery of HAT-P-67 b. These observations were carried out by KeplerCam on the Fred Lawrence Whipple Observatory

(FLWO) 1.2m telescope and consist of 6 observations ranging from April 2011 to May 2013.[5]

From the published magnitudes, we calculate the relative fluxes as well as flux uncertainties, and normalize each observation's out-of-transit baseline flux to unity. Although the published data only contain magnitudes and no external parameters for detrending the data (e.g., airmass or full width at half maximum), the data quality is sufficiently high such that upon including `celerite`'s quasi-periodic Gaussian process (GP) (Foreman-Mackey et al. 2017) in our fits, we are largely able to match the precision reached by Z17.

Similar to the HATNet data, these data were collected in two bandpasses. The first five observations were obtained using the Sloan-i filter, whereas the last observation used the Sloan-z filter. Additionally, the six follow-up observations were obtained with slightly different exposure times. Though treating each night of data as collected by a different instrument nominally results in better log-evidence (see Table 2), there was no observed improvement in the uncertainty of parameters and thus does not justify the doubling of the number of parameters (from 9 to 19) and the corresponding increase in computation time.

2.5. *TESS Photometry*

The Transiting Exoplanet Survey Satellite (TESS, Ricker et al. 2014) is an all-sky transit survey designed to observe planets transiting the nearest and brightest stars. TESS observed HAT-P-67 b in its 2-minute cadence mode in eight sectors (Sectors 24, 26, 51, 52, 53, 78, 79, and 80) between April 2020 and July 2024, all after the initial discovery in 2017. In total, 35 full and three partial transits were observed.

We downloaded these data from the Mikulski Archive for Space Telescopes (MAST[6]) in the form of Pre-search Data Conditioning Simple Aperture Photometry (PDCSAP) light curves. This data has been corrected for instrumental systematics as well as photometric dilution by nearby sources, and a visual inspection of all sectors finds that no additional data removal is warranted. Additionally, we find that fitting all sectors of TESS with joint parameters for instrumental jitter and median flux results in the highest log-evidence as well as eight fewer parameters than stratifying by sector (see Table 2).

The high photometric precision of TESS, when combined with the datasets mentioned above, allows us to place more stringent constraints on the transit parameters. In addition, one important advantage offered by TESS is its continuous, high-precision out-of-transit monitoring which allows us to characterize stellar activity. We identify clear modulation in the light curve on the order of a fraction to a few parts per thousand which allows us to estimate the stellar rotation period of the star (see §3.2.1). This proves to be especially useful for this system, which has high scatter in the RVs due to the active, fast-rotating host. Whereas HATNet (see §2.3) does provide out-of-transit monitoring, its precision of a few milli-magnitudes is not high enough to characterize this activity. On the other hand, ground-based follow-up (§2.4) provides higher precision light curves but only for in-transit portions. Thus, besides offering improved uncertainties on planetary parameters as compared to previous data, TESS also offers a new perspective, allowing us to measure the stellar rotation period of the host star and gain a more robust understanding of the system.

3. ANALYSIS

3.1. *Stellar Properties*

Knowledge of the host star's fundamental properties is crucial to transforming our differential measurements into physical quantities. The release of the Gaia DR3 parallax for the system also motivates a re-analysis of the host star. We inferred the fundamental and photospheric stellar parameters of HAT-P-67 A using the `isochrones` (Morton 2015) package, executing a simultaneous Bayesian fit of the Modules for Experiments in Stellar Evolution (MESA; Paxton et al. 2011, 2013, 2018, 2019; Jermyn et al. 2023) Isochrones & Stellar Tracks (MIST; Dotter 2016; Choi et al. 2016) isochrone grid to a curated collection of data for the star with the nested sampler `MultiNest` (Feroz & Hobson 2008; Feroz et al. 2009, 2019). We fit the MIST grid to

1. Galaxy Evolution Explorer (GALEX) GUVcat_AIS FUV photometry including in quadrature its zero-point uncertainty of 0.02 mag (Bianchi et al. 2017);

2. Gaia DR2 G photometry including its zero-point uncertainty of 0.0018 mag (Gaia Collaboration et al. 2016, 2018; Arenou et al. 2018; Busso et al. 2018; Evans et al. 2018; Riello et al. 2018);

3. Tycho-2 B_T and V_T photometry including in quadrature their zero-point uncertainties (0.078, 0.058) mag (Høg et al. 2000; Maíz-Apellániz 2005);

4. Two-micron All-sky Survey (2MASS) JHK_s photometry. The 2MASS Point Source Catalog

[5] See §2.1 of Z17 for a detailed description of these photometric observations.

[6] https://mast.stsci.edu/portal/Mashup/Clients/Mast/Portal.html

`?_msigcom` photometric uncertainties we use, presented in Skrutskie et al. (2006), already includes zero-point uncertainties.

5. Wide-field Infrared Survey Explorer (WISE) CatWISE2020 $W1$ and $W2$ photometry including in quadrature their zero-point uncertainties (0.032, 0.037) mag[7] (Wright et al. 2010; Mainzer et al. 2011; Eisenhardt et al. 2020; Marocco et al. 2021);

6. a zero point-corrected Gaia DR3 parallax (Gaia Collaboration et al. 2021; Fabricius et al. 2021; Lindegren et al. 2021a,b; Rowell et al. 2021; Torra et al. 2021); and

7. an estimated extinction value based on a three-dimensional extinction map (Lallement et al. 2022; Vergely et al. 2022).

As priors we use

1. a Chabrier (2003) log-normal mass prior for $M_* < 1\ M_\odot$ joined to a Salpeter (1955) power-law prior for $M_* \geq 1\ M_\odot$;

2. a metallicity prior based on the Geneva-Copenhagen Survey (GCS; Casagrande et al. 2011);

3. a log-uniform age prior between 1 Gyr and 10 Gyr;

4. a uniform extinction prior in the interval 0 mag $< A_V <$ 0.5 mag; and

5. a distance prior proportional to volume between the Bailer-Jones et al. (2021) geometric distance minus/plus five times its uncertainty.

The results of these analyses are shown in Table 3 and Figure A3.

Table 3. Adopted stellar parameters.

Property (Unit)	Value
Observed Quantities	
GALEX FUV	19.74 ± 0.13
Gaia DR2 G	9.975 ± 0.002
Tycho B_T	10.629 ± 0.087
Tycho V_T	10.158 ± 0.067
2MASS J	9.145 ± 0.021
2MASS H	8.961 ± 0.019
2MASS Ks	8.900 ± 0.019
CatWISE $W1$	8.862 ± 0.033
CatWISE $W2$	8.877 ± 0.038
Gaia DR3 parallax (mas)	2.701 ± 0.010
Isochrone-inferred parameters[a]	
Effective temperature $T_{\rm eff}$ (K)	6640^{+140}_{-130}
Surface gravity $\log(g)$ (cm s^{-2})	3.84 ± 0.03
Metallicity [Fe/H]	$0.14^{+0.14}_{-0.12}$
Mass M_* ($M_\odot$)	1.73 ± 0.10
Radius R_* ($R_\odot$)	2.62 ± 0.03
Luminosity L_* ($L_\odot$)	$11.96^{+0.84}_{-0.73}$
Age $\tau_{\rm iso}$ (Gyr)	$1.46^{+0.29}_{-0.26}$
Distance (pc)	370.1 ± 1.3

NOTE—Reported uncertainties for observed parameters are total (see §3.1). Isochrone-inferred parameters report the median and $1\,\sigma$ standard deviation drawn from the sampled posterior distribution. a: This work.

3.2. *Photometry*

Following §2.3, 2.4, and 2.5, we reached the following conclusions:

- using all three sources of photometric data (HATNet, TESS, and KeplerCam) results in the best constraints and most robust fit;
- HATNet data should be treated as two separate instruments, with different jitter and relative flux offsets for each bandpass;
- KeplerCam data should be treated as a single instrument, encompassing all six follow-up light curves; and
- all eight sectors of TESS data should also be treated as a single instrument, with the same jitter and flux offset values.

Although the ephemeris of HAT-P-67 b is already well-constrained from Z17, our analysis includes the addition of the later TESS data, and thus we want to ensure that the priors for our joint fits encompass the updated P and t_0 values. We performed a fit in `juliet` following the above points, and obtain $P = 4.8101076 \pm 0.0000011$ days and $t_0 = 2459010.99177 \pm 0.00017$ which are consistent with those from Z17.

3.2.1. *Stellar Activity From TESS*

We aim to use TESS photometry to inform our model of the stellar activity in the RVs. From TESS, we observe quasi-periodic out-of-transit variability (see Figure

[7] https://wise2.ipac.caltech.edu/docs/release/allsky/expsup/sec4_4h.html#PhotometricZP

A1). This variability is most obvious in the latter half of Sector 24 and in all of Sector 26. The amplitude of the variability is significantly less in Sectors 51 and 52. The activity returns to an elevated level after two years, during Sectors 78 through 80. With these clues, our original suspicion was that these arise from stellar activity due to starspots and/or faculae rotating in and out of view, and with said features having lifetimes on the order of the length of one TESS sector ($\sim 10-100$ days). To test this hypothesis, we plot the Lomb-Scargle periodogram (Lomb 1976; Scargle 1982) of the TESS data, removing data within 0.05 in phase ($\sim$ 5.8 hours) on both sides of each transit center to avoid capturing the transiting planetary signal. The periodogram is shown in Figure 2, where we find that the variability has a period of ~ 5 days.

We observe the strongest peak (false-alarm probability $< 0.1\%$) at 5.40 ± 0.09 days, where we obtain the uncertainty by fitting the peak with a Gaussian. Furthermore, upon phasing the photometry at this period, we measure an amplitude of 274 ± 5 parts per million (ppm). The phase-folded data is shown in Figure 3 and allows us to see the modulation. We believe this signal is due to stellar rotation, as upon conducting a periodogram analysis of Sector 26 data only, the sector which visually exhibits the strongest variability, we can recover the signal, with the strongest peak at 5.394 days. Additionally, we find the strength of the signal decreases in Sectors 51 through 53 (see the full photometry in Figure A1).

Accounting for macroturbulence and instrumental broadening in addition to rotational broadening, Z17 finds $v \sin i_* = 30.9 \pm 2.0$ km/s and a macroturbulence of 9.22 ± 0.5 km/s for HAT-P-67 from HIRES spectra. Given the radius of HAT-P-67 ($R_* = 2.62 \pm 0.03\ R_\odot$), a 5.4-day rotation period corresponds to $v = 24$ km/s (consistent with the above value to 3σ), assuming the stellar axis is approximately aligned with the plane of the sky. This assumption is justified as the planet has $i = 85.0°$, close to 90°, and Z17 measure through Doppler tomography that the system is spin-orbit aligned to within 12°, for a maximum deviation of 17°. Thus, our results suggest that more of the spectral line broadening is due to macroturbulence than found by Z17. In other words, their macroturbulence estimate is low, leading to a $v \sin i_*$ measurement that is higher than ours by 3σ. HAT-P-67's rotation period is as expected for a star of its mass that is evolving off the main sequence (van Saders & Pinsonneault 2013).

3.2.2. *Variability at Planetary Period*

We note that in Figure 2, despite having removed the primary transits from the data before constructing the periodogram, there is an additional, weaker peak at the period of the planet, which demonstrates that while the stellar rotation signal dominates the out-of-transit variability, there may be additional signs of variation such as a phase curve induced by HAT-P-67 b or secondary eclipses within the data. To test this, we phased the entire TESS light curve (including in-transit as well as out-of-transit) to the planetary period. We observe moderate phase curve modulations, but do not find clear evidence for a secondary. Reconstructing the periodogram in Figure 2 while excluding data within phase 0.05 of a hypothetical eclipse at phase 0.5 shows the same peak at 4.81 days, which is consistent with the lack of an observable secondary. We similarly did not find eclipse measurements of this target described in the literature.

This is in agreement with theoretical calculations: given $R_p/R_* = 0.0823$, $T_* = 6417^{+102}_{-143}$ K, and $T_p = 1903 \pm 25$ K (Z17), the luminosity ratio between HAT-P-67 b and HAT-P-67 is 5.29×10^{-5}, for a secondary depth of 53 ppm. While binning of 400 points allows us to reach a median errorbar of 52.6 ppm, there are too many variations of a few hundred ppm in the out-of-transit light curve that make it difficult to discern a secondary. Furthermore, the phase curve in Figure 4 exhibits steep ramps on both sides of primary transit, unlike traditional phase curves (e.g., Daylan et al. 2021), which explains the power we observe at the planet period. We conclude that we may be observing signs of magnetic interactions between the star and planet, although a thorough analysis is outside the scope of this work (but see §4.2).

3.2.3. *Transit Timing Variations*

As there may be interactions between the star and planet (§4.2), we search for orbital decay for HAT-P-67 b. We combine all transits observed by KeplerCam and TESS and fit each with an independent mid-time of transit. We exclude data from HATNet as its time resolution is insufficient to detect transits over a single orbital period. We define Gaussian priors for t_0 for each transit observed in the data, with medians equal to the predicted transit times assuming a linear ephemeris and standard deviations of 0.1 day. The observed minus calculated transit times are plotted in Figure 5. We do not detect any significant timing variations on either short or long timescales, but this does not place significant constraints on the multiplicity of this system.

3.3. *NEID Radial Velocities*

3.3.1. *Periodogram of RVs*

To confirm the presence of the 4.8-day signal and to search for additional signals, we computed the $l1$ periodogram (Hara et al. 2016), which is an implementation

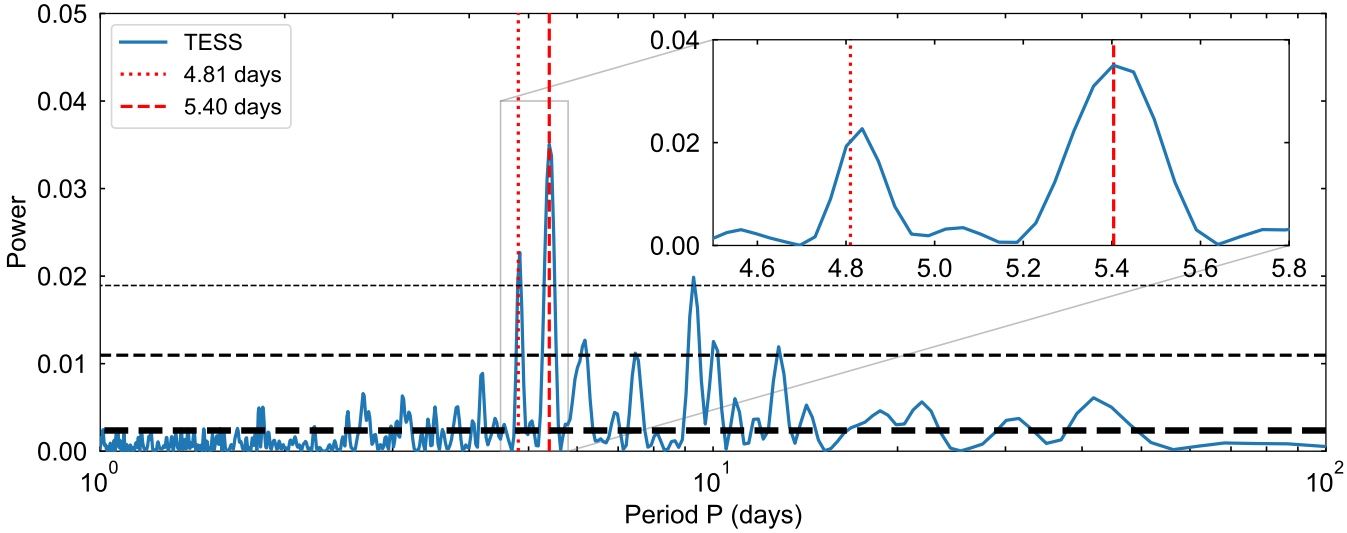

Figure 2. Periodogram of out-of-transit data from TESS (blue line). The Lomb-Scargle periodogram is designed to identify periodic signals within unevenly spaced data. Vertical red lines are drawn to indicate the period of the planet, 4.81 days, and the suspected stellar rotation period of 5.40 ± 0.09 days. The horizontal lines represent 10%, 1%, and 0.1% false-alarm levels calculated from 100 random draws. The inset shows the uncertainty on the stellar rotation peak and demonstrates that the data can conclusively resolve the stellar rotation and planetary signals. There is a signal at the planet's period even though its primary transits have been removed before calculating this periodogram.

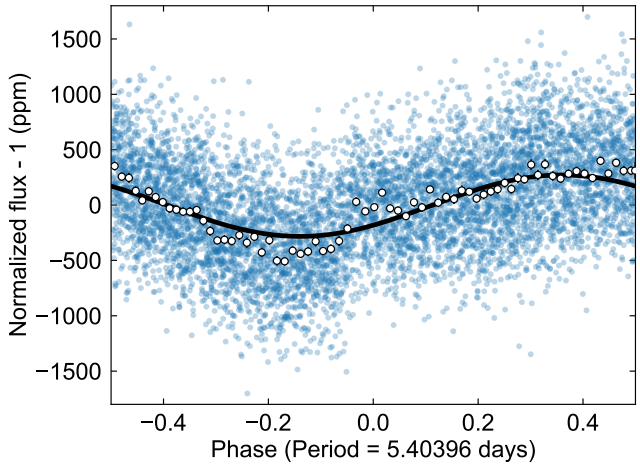

Figure 3. Out-of-transit data from TESS phased to the strongest peak of 5.40 days. Blue points represent raw data binned by 10, and white circles represent bins of 1000. The best-fit sinusoidal model phased to the Lomb-Scargle peak is overplotted in black.

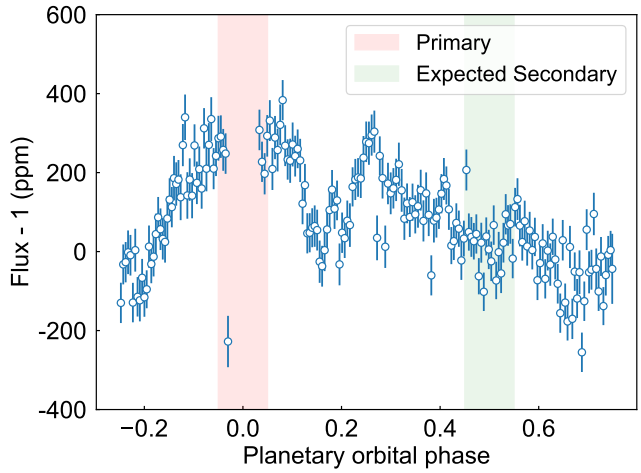

Figure 4. Light curve for HAT-P-67 from TESS, phased to the planetary orbital period. Each point here is the result of binning 400 2-minute cadence points in the TESS photometry. The light curve was first phase-folded then binned.

of the Least Angle Regression (LARS) algorithm (Efron et al. 2004) and designed to search for planets using RVs. The $l1$ periodogram is more robust against aliasing than the Lomb-Scargle periodogram, thus resulting in fewer peaks, and aims to represent RV data as a sum of a few sinusoidal signals. The periodogram is plotted in Figure 6, with the periods of peaks with Bayes factors of ≥ 2.0 labeled. The signal of the planet, ≈ 4.7 days, is clearly represented. A signal of roughly half the planet period is present, although it is slightly less than half the planet period and is not significant (p-value of 0.285). These suggest that it is either an alias of the planetary signal or a spurious signal. Additionally, there is a peak around $P = 38$ days, but it is not immediately obvious whether this is a true frequency or an alias.

3.3.2. *Two-Planet Fit*

Another method commonly used to search for additional signals in radial velocities is to perform a fit to

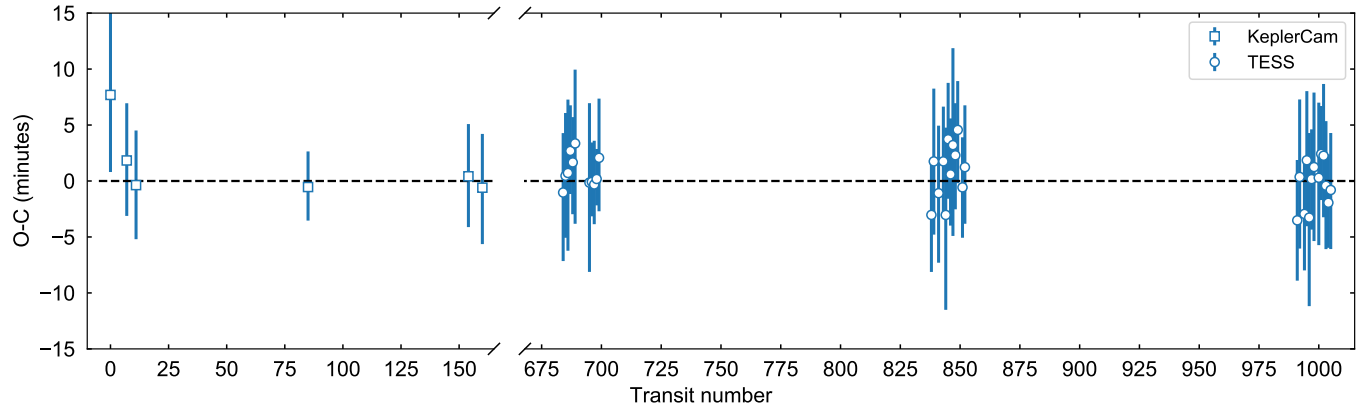

Figure 5. O-C plot of mid-transit times. No significant short- or long-term deviations are found.

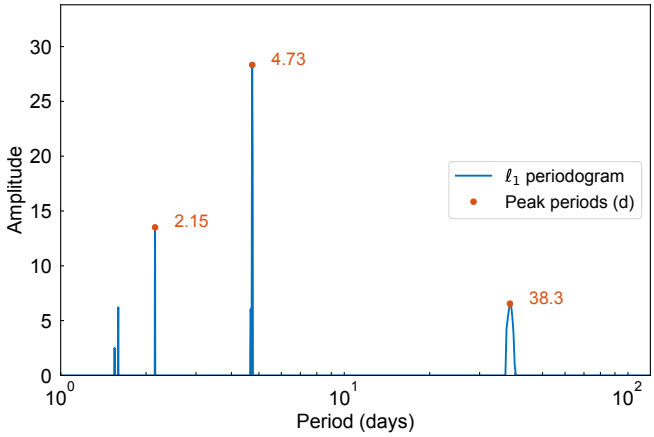

Figure 6. $l1$ periodogram for HAT-P-67 radial velocities. Labeled in orange are the periods of the peaks with Bayes factors ≥ 2.0. The Bayes factors of the signals, in order of increasing period, are 6.7, 10.3, and 2.0 respectively. The p-values of the peaks are 2.85×10^{-1}, 2.55×10^{-2}, and 1.48×10^{-4} respectively.

the data including an extra planet, while allowing the period of the hypothetical planet to take on values in a broad, uniform range (e.g., Espinoza et al. 2019b). To do this, we used the posteriors for P and t_0 from our photometric fit as the priors for our first planet, effectively constraining the ephemeris of the known planet, and included a second planet with a free period. Specifically, we defined the period with a uniform prior between 1.0 and 60 days, as the largest continuous time span of our radial velocities is from February 2023 to July 2023 ($\sim$ 120 days). We reason that it is justified to search for signals with periods half this length, but not more. We also define the t_0 prior for the second planet to be uniform, starting from the first data point and ending 60 days later. Both "planets" were assumed to have circular orbits.

Our results return $P = 5.048 \pm 0.660$ days for the second planet, with the posterior distribution exhibiting a single large peak at $P = 5.05$ days and isolated, weaker peaks at $P = 5.12$ and 13.0 days. It should be noted that this two-planet fit performs nominally better than the single, 4.8-day planet fit, with a log-evidence that is higher by 9.8 (-498.193 vs -507.982), despite having five more parameters. Statistically, this is "strong" evidence that there is an additional signal in the system, with the two-planet fit being 1.8×10^4 times more likely.

However, it is physically improbable for HAT-P-67 to harbor two planets with periods of $P = 4.81$ and $P = 5.05$ days, as two such planets would be within each others' Hill radii. Instead, we note the close proximity of this second period with the period of out-of-transit variability obtained by TESS ($P = 5.40 \pm 0.09$ days) and attribute these to originate from a single physical process. Interestingly, upon repeating the same fit on the first 66 of 75 RV points (analogous to a cross-validation test; e.g., Blunt et al. 2023), the posterior distribution of P exhibits a cluster of peaks around $P = 5.05$ days but also a larger cluster around $P = 5.6$ days. We interpret this as an indication that the period of the second signal in the data is not well-constrained by the RVs, but its range of values encompasses the signal seen in the photometry. Finally, upon repeating the two-planet fit and disallowing Hill sphere crossings, we obtain periods of $1.82^{+0.87}_{-0.42}$ and $12.95^{+0.40}_{-0.09}$ days. However, the log-evidences of these fits are significantly lower than for a single-planet fit, suggesting there is no evidence for planets at these periods. Combining the conclusions independently deduced from the photometry and RVs, we believe that it is justified to use a physically-motivated GP (Nicholson & Aigrain 2022) when fitting the RVs in order to account for contamination from stellar activity (e.g., Espinoza et al. 2019b, 2022).

3.3.3. *Stellar Activity Indicators*

A total of 10 stellar activity indicators are calculated by the SERVAL pipeline (Zechmeister et al. 2018).

These are the differential line width (dLW), chromatic RV index (CRX), calcium infrared triplet (CaIRT), Hα, sodium D and near-infrared doublets, and Paschen delta indicators (defined in Zechmeister et al. 2018). We plot these activity indicators against the radial velocities in Figure 7. We calculate the Spearman rank correlation coefficient ρ between each indicator and the RVs, which tests for monotonic relationships between the two variables. We find that dLW yields $\rho = 0.293$, corresponding to $p = 0.011$, demonstrating that the changing line width has a significant, positive correlation with the measured radial velocities and likely creates the observed scatter. It is worth noting that ρ ignores the exact values of the data and only depends on the ranks of each variable, explaining why it is difficult to discern a trend from the dLW-RV panel in Figure 7. We also find statistically significant correlations with the Paschen delta and sodium near-infrared doublet indicators.

3.4. *NEID + HIRES Radial Velocities*

Before we jointly fit the radial velocities with photometry, we conducted a few more analyses using all available radial velocity data to determine which parameters to fit for in our joint models. In particular, we investigate long-term linear trends and eccentricity.

3.4.1. *Linear Models*

Due to the presence of a co-moving, wide-binary companion HAT-P-67 b at 3400 AU (Mugrauer 2019; Gully-Santiago et al. 2024), we test the possibility that there is a long-term linear trend in the radial velocity data. We fit using `juliet` a linear model to the radial velocity data with time as the regressor. However, the inclusion of such a model does not yield an increase in model log-evidence, nor are there significant non-zero linear terms (the posterior values for slope are consistent with zero). We conclude that HAT-P-67 b is too far away to cause a significant signal in the RVs within a period of ~ 10 years and do not use a linear model elsewhere in our modeling.

3.4.2. *Eccentricity*

We also test the possibility that HAT-P-67 b may have an eccentric orbit by placing wide uniform priors on e and ω. However, the posterior distributions are skewed towards zero eccentricity, suggesting that the data do not provide constraints on e. Z17 reached similar conclusions based on their Doppler tomography and radial velocity results, and although we have additional data, we do not expect them to place constraints on e due to our sampling scheme; eccentricity measurements are most constraining when sampling throughout the planet orbital phase. Nonetheless, due to the short orbital period of the planet, as well as the tidal circularization timescale of ~ 1 Gyr (Dobbs-Dixon et al. 2004), we do not believe it to have a significant eccentricity. Including the additional e and ω parameters also does not increase the log-evidences of the fits, and thus for the purposes of our data modeling we fix the orbit to be circular in our final fits.

3.5. *Global Analysis*

3.5.1. *No Gaussian Process*

Having gained an understanding of the photometric and RV data separately, we are now in a position to conduct joint fitting of this system including all datasets. Joint fitting gives self-consistent measurements of the system parameters, allowing us to derive HAT-P-67 b's density. We first conduct a joint fit which does not use a Gaussian process, and instead only includes planetary parameters for a single planet and instrumental nuisance parameters. Since we have demonstrated that the host star exhibits activity, we do not expect this fit to be the best fit to the data, and will also likely yield underestimated uncertainties. Nonetheless, it serves as a good baseline to which we can compare other models. We carry out our sampling using the `dynesty` (Speagle 2020) dynamic nested sampler to increase sampling efficiency. The priors and posteriors for each applicable parameter are listed in Table 4. The best-fit RV model is shown in Figure 8 and on the left panel in Figure 9.

3.5.2. *Quasi-Periodic Gaussian Process*

We next add `celerite`'s quasi-periodic Gaussian process, which consists of both quasi-periodic and exponential components. This is physically motivated by our previous analyses which show that the host star likely rotates at a period similar to the planet's orbital period. The priors for this fit are displayed in Table 4. To summarize, we take the best-fit values from our photometry-only fit (see §3.2) for P and t_0, and expand the standard deviation by a factor of 100 to ensure we capture the true values. We allow R_p/R_*, b, q_1, and q_2 to vary uniformly between 0 and 1. Additionally, we implement a normal prior of 5.4 ± 0.1 days on the period of the quasi-periodic component of the GP, as a result of our analyses in §3.2 and 3.3. We find that this prior is able to capture the stellar rotation period while excluding the planetary period. We implement broad log-uniform priors on the remaining hyperparameters of the GP (amplitude, additive factor, and exponential length-scale). A description of the hyperparameters can be found in Espinoza et al. (2019a).

The unphased and phased radial velocities are shown in Figures 8 and 9 respectively. The phased and fitted

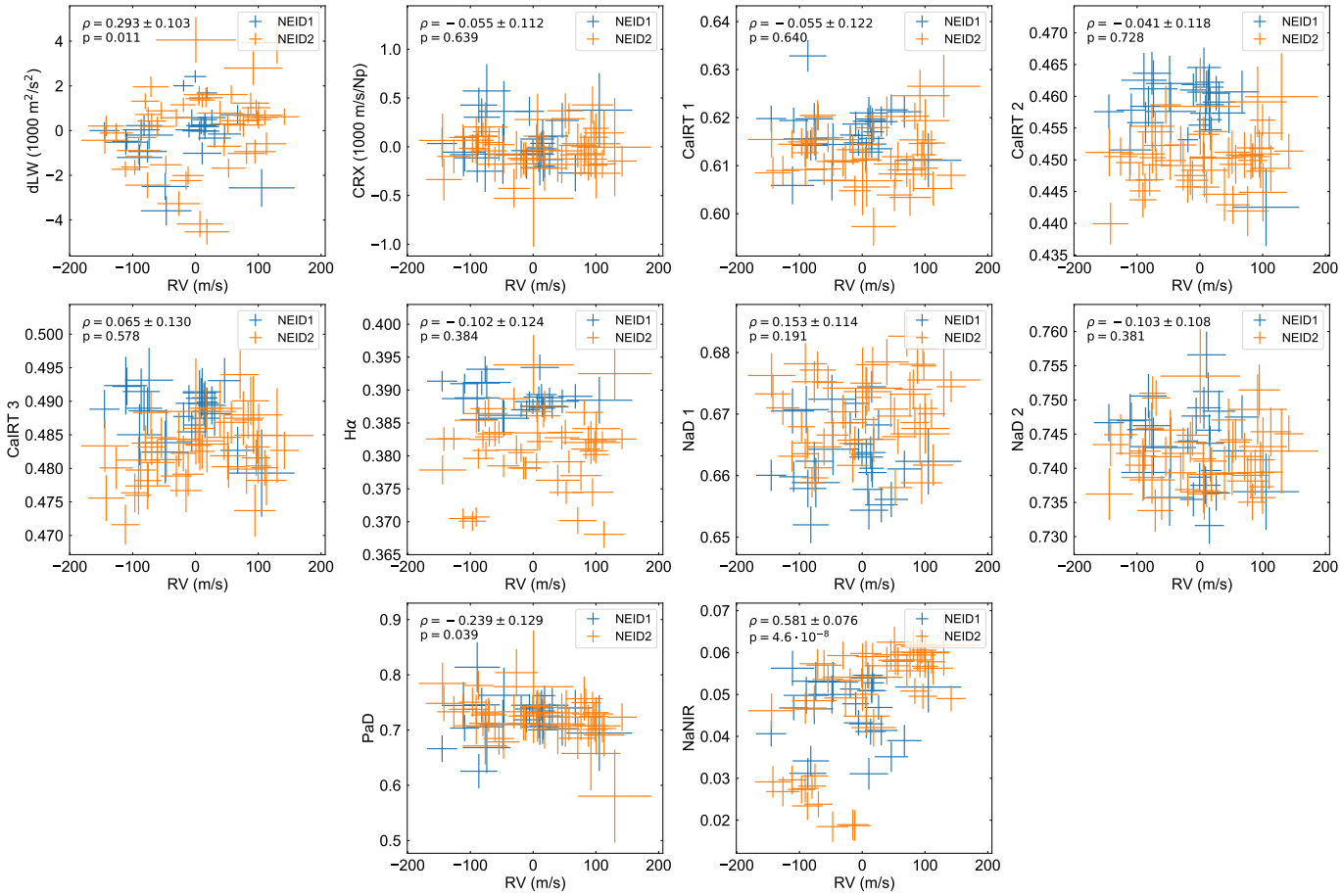

Figure 7. Correlations between the radial velocities and stellar activity indicators dLW, CRX, CaIRT, Hα, NaD, PaD, and NaNIR (defined in Zechmeister et al. 2018). NEID1 data is plotted in blue and NEID2 data in orange. The data from NEID1 and NEID2 are normalized to their respective zero-points. We calculate the uncertainties of the Spearman correlation coefficients using bootstrap resampling. The differential line width, Paschen delta, and sodium near-infrared indicators have statistically significant ($p < 0.05$) monotonic correlations with the radial velocities, with $\rho = 0.293 \pm 0.101$, -0.239 ± 0.129 and 0.581 ± 0.076 as obtained from a Spearman rank correlation test. A visual trend is not always immediately apparent due to the rank correlation test ignoring the actual values of the data.

photometry is shown in Figure 10. We find that the log-evidences are greatly increased upon using a quasi-periodic GP as compared to using no GP (747223 vs 730107, or $\Delta \ln Z = 17116$). The posteriors are listed in Table 4 and the corner plot is shown in Figure A2.

3.5.3. *Uncertainty Comparison*

The uncertainty on the RV semi-amplitude is increased from 19% (43 ± 8 m/s) to 33% (38^{+12}_{-13} m/s) upon including a Gaussian process; we believe this larger uncertainty more accurately reflects unknown noise sources in the data. In particular, upon inclusion of a GP, the jitter values have decreased significantly (from $40.9^{+9.4}_{-7.9}$ m/s to $4.6^{+7.9}_{-3.0}$ m/s for NEID1, and from $60.9^{+8.5}_{-6.7}$ m/s to $2.9^{+3.5}_{-1.5}$ m/s for NEID2). Together with the increase in uncertainty on K, we interpret this to indicate the uncertainties of the model have been correctly inflated to account for the excess discrepancies between the data and model, rather than inflating the data uncertainties.

4. DISCUSSION

4.1. *Implications for HAT-P-67 b*

Our revised mass measurement of $M_p = 0.45 \pm 0.15$ M_J is consistent with the previous upper-limit of $M_p < 0.59$ M_J obtained by Z17. When combined with our updated stellar mass calculation, this yields $\rho_p = 0.061^{+0.020}_{-0.021}$ g cm^{-3}, also consistent with $\rho_p = 0.052^{+0.039}_{-0.028}$ g cm^{-3} from Z17 and with a smaller uncertainty. The mass uncertainty of 33% places the object in a region where the mass uncertainty and spectroscopic data quality have comparable contributions to uncertainty in inferred atmospheric properties from transmission spectroscopy, and lies in the regime between initial

Table 4. Priors and posteriors for joint fit of HAT-P-67 b.

Parameter	Prior	QP GP Posterior	No GP Posterior	Description
Planetary Parameters				
P	$\mathcal{N}(4.8101, 0.0001)$	$4.81010690^{+0.00000070}_{-0.00000068}$	$4.81010827^{+0.00000058}_{-0.00000059}$	Orbital period (days)
t_0	$\mathcal{N}(2011.0, 0.1)$	$2010.99174^{+0.00017}_{-0.00016}$	$2010.99156^{+0.00015}_{-0.00014}$	Transit center ($\mathrm{BJD_{TDB}} - 2457000$)
R_p/R_*	$\mathcal{U}(0.0, 1.0)$	$0.08200^{+0.00025}_{-0.00026}$	$0.08059^{+0.00028}_{-0.00025}$	Planet-star radius ratio
b	$\mathcal{U}(0.0, 1.0)$	$0.460^{+0.017}_{-0.019}$	$0.433^{+0.023}_{-0.024}$	Impact parameter
a/R_*	$\mathcal{J}(1.0, 100.0)$	$5.173^{+0.049}_{-0.046}$	$5.273^{+0.059}_{-0.058}$	Scaled semi-major axis
e	Fixed, 0.0	—	—	Eccentricity
ω	Fixed, 90.0	—	—	Argument of periastron (°)
K	$\mathcal{U}(0.0, 1000.0)$	38^{+12}_{-13}	43 ± 8	Semi-amplitude (m/s)
M_p	—	0.45 ± 0.15	—	Mass ($\mathrm{M_J}$)
R_p	—	2.140 ± 0.025	—	Radius ($\mathrm{R_J}$)
ρ_p	—	$0.061^{+0.020}_{-0.021}$	—	Density (g cm^{-3})
Photometric Parameters				
D_{HATNet}	$\mathcal{U}(0.0, 1.0)$	$0.752^{+0.028}_{-0.027}$	$0.770^{+0.030}_{-0.028}$	Dilution factor for HATNet
F_{TESS}	$\mathcal{N}(0.0, 0.1)$	-90 ± 170	-89 ± 3	Relative flux offset (ppm)
$F_{\mathrm{KeplerCam}}$	$\mathcal{N}(0.0, 0.1)$	150 ± 340	173^{+48}_{-50}	Relative flux offset (ppm)
F_{HATNet}	$\mathcal{N}(0.0, 0.1)$	-90^{+770}_{-800}	-13 ± 65	Relative flux offset (ppm)
$\sigma_{w,\,\mathrm{TESS}}$	$\mathcal{J}(10^{-5}, 10^5)$	$0.014^{+1.231}_{-0.014}$	$479.5^{+4.4}_{-4.5}$	Jitter term for TESS (ppm)
$\sigma_{w,\,\mathrm{KeplerCam}}$	$\mathcal{J}(10^{-5}, 10^5)$	2746^{+30}_{-32}	3019 ± 36	Jitter term for KeplerCam (ppm)
$\sigma_{w,\,\mathrm{HATNet}}$	$\mathcal{J}(10^{-5}, 10^5)$	4450^{+33}_{-32}	4466 ± 34	Jitter term for HATNet (ppm)
q_1	$\mathcal{U}(0.0, 1.0)$	$0.173^{+0.026}_{-0.024}$	$0.159^{+0.030}_{-0.027}$	First limb-darkening coefficient
q_2	$\mathcal{U}(0.0, 1.0)$	$0.29^{+0.08}_{-0.07}$	$0.38^{+0.10}_{-0.09}$	Second limb-darkening coefficient
B_{TESS}	$\mathcal{J}(10^{-6}, 10^6)$	$1.04^{+0.06}_{-0.03}$	—	Amplitude of GP (10^{-6} ppm)
$B_{\mathrm{KeplerCam}}$	$\mathcal{J}(10^{-6}, 10^6)$	$1.92^{+0.75}_{-0.47}$	—	Amplitude of GP (10^{-6} ppm)
B_{HATNet}	$\mathcal{J}(10^{-6}, 10^6)$	$1.31^{+0.71}_{-0.24}$	—	Amplitude of GP (10^{-6} ppm)
C_{TESS}	$\mathcal{J}(10^{-4}, 10^4)$	$2.4^{+2.9}_{-1.7}$	—	Additive factor for GP amplitude
$C_{\mathrm{KeplerCam}}$	$\mathcal{J}(10^{-4}, 10^4)$	$0.42^{+216.37}_{-0.42}$	—	Additive factor for GP amplitude
C_{HATNet}	$\mathcal{J}(10^{-4}, 10^4)$	$0.25^{+14.70}_{-0.24}$	—	Additive factor for GP amplitude
L_{TESS}	$\mathcal{J}(10^{-3}, 10^3)$	$5.03^{+0.38}_{-0.29}$	—	Exponential length-scale
$L_{\mathrm{KeplerCam}}$	$\mathcal{J}(10^{-3}, 10^3)$	$0.075^{+0.038}_{-0.022}$	—	Exponential length-scale
L_{HATNet}	$\mathcal{J}(10^{-3}, 10^3)$	290^{+360}_{-170}	—	Exponential length-scale
$P_{\mathrm{rot,\,TESS}}$	$\mathcal{N}(5.4, 0.1)$	5.39 ± 0.09	—	Period for QP component (days)
$P_{\mathrm{rot,\,KeplerCam}}$	$\mathcal{N}(5.4, 0.1)$	5.38 ± 0.09	—	Period for QP component (days)
$P_{\mathrm{rot,\,HATNet}}$	$\mathcal{N}(5.4, 0.1)$	5.35 ± 0.07	—	Period for QP component (days)
RV Parameters				
μ_{NEID1}	$\mathcal{U}(-200, 200)$	-25^{+31}_{-30}	-28 ± 10	RV zero-point for NEID1 (m/s)
μ_{NEID2}	$\mathcal{U}(-200, 200)$	$24^{+19}-20$	23 ± 10	RV zero-point for NEID2 (m/s)
μ_{HIRES}	$\mathcal{U}(-200, 200)$	15^{+28}_{-26}	15 ± 19	RV zero-point for HIRES (m/s)
σ_{NEID1}	$\mathcal{J}(1.0, 1000.0)$	$4.6^{+7.9}_{-3.0}$	$40.9^{+9.4}_{-7.9}$	Jitter term for NEID1 (m/s)
σ_{NEID2}	$\mathcal{J}(1.0, 1000.0)$	$2.9^{+3.5}_{-1.5}$	$60.9^{+8.5}_{-6.7}$	Jitter term for NEID2 (m/s)
σ_{HIRES}	$\mathcal{J}(1.0, 1000.0)$	30^{+32}_{-20}	75^{+18}_{-14}	Jitter term for HIRES (m/s)
$B_{\mathrm{NEID1+NEID2}}$	$\mathcal{J}(1.0, 10^6)$	4200^{+1900}_{-1200}	—	Amplitude of GP (m/s)
B_{HIRES}	$\mathcal{J}(1.0, 10^6)$	5300^{+5600}_{-3600}	—	Amplitude of GP (m/s)
$C_{\mathrm{NEID1+NEID2}}$	$\mathcal{J}(0.01, 100)$	$0.4^{+6.4}_{-0.3}$	—	Additive factor for GP amplitude
C_{HIRES}	$\mathcal{J}(0.01, 100)$	$3.5^{+31.4}_{-3.4}$	—	Additive factor for GP amplitude
$L_{\mathrm{NEID1+NEID2}}$	$\mathcal{J}(1.0, 100)$	$4.1^{+7.7}_{-2.6}$	—	Exponential length-scale
L_{HIRES}	$\mathcal{J}(1.0, 100)$	$10.6^{+25.2}_{-7.7}$	—	Exponential length-scale
$P_{\mathrm{rot,\,NEID1+NEID2}}$	$\mathcal{N}(5.4, 0.1)$	5.39 ± 0.09	—	Period for QP component (days)
$P_{\mathrm{rot,\,HIRES}}$	$\mathcal{N}(5.4, 0.1)$	5.39 ± 0.09	—	Period for QP component (days)

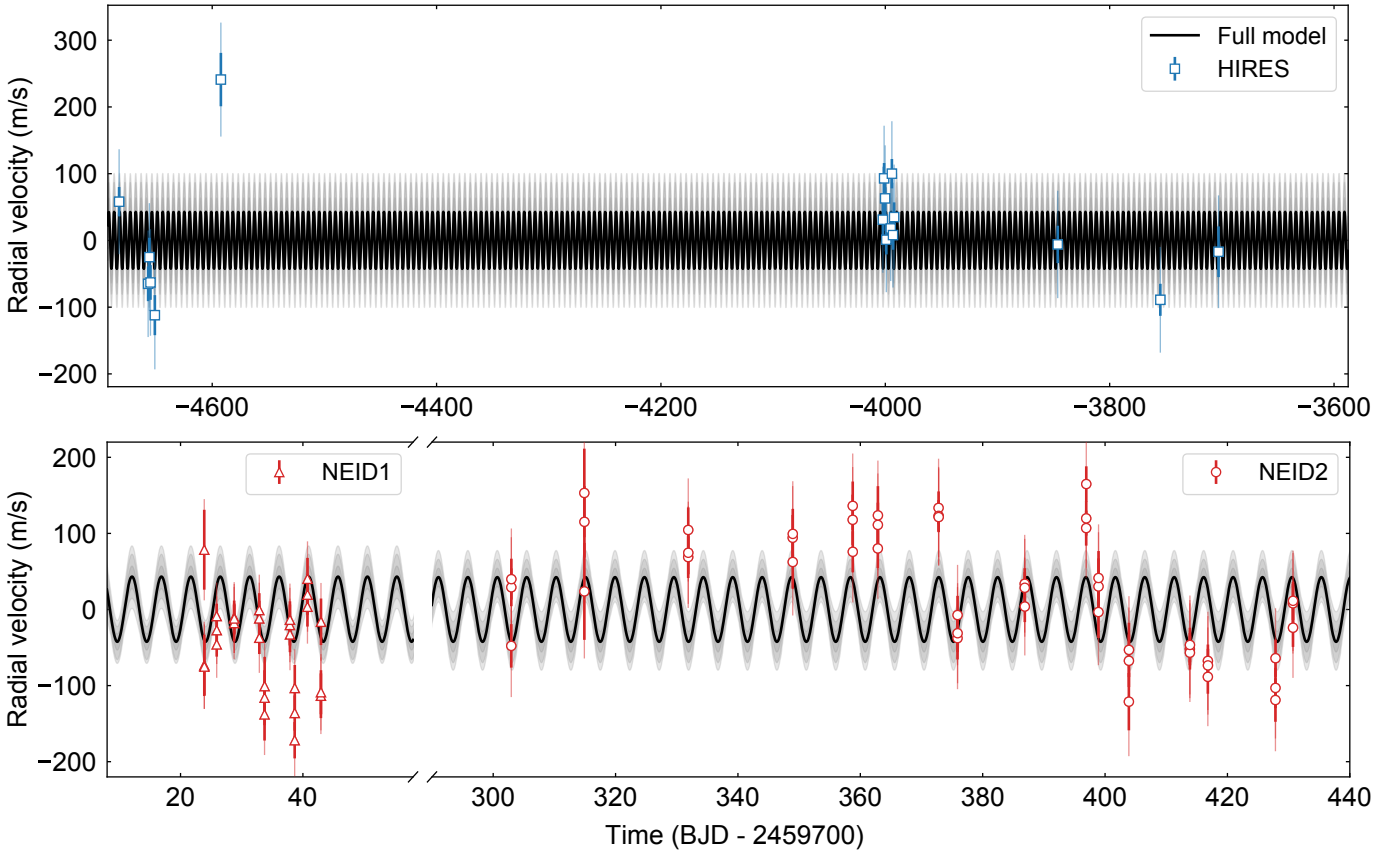

Figure 8. Radial velocity data points with overplotted model containing one Keplerian. The gray bands represent 68%, 95%, and 99% confidence intervals. The data uncertainties are drawn as bold errorbars, and the thin errorbars represent the jitter added in quadrature to the data uncertainties. This model does not include a Gaussian process, resulting in large jitter values.

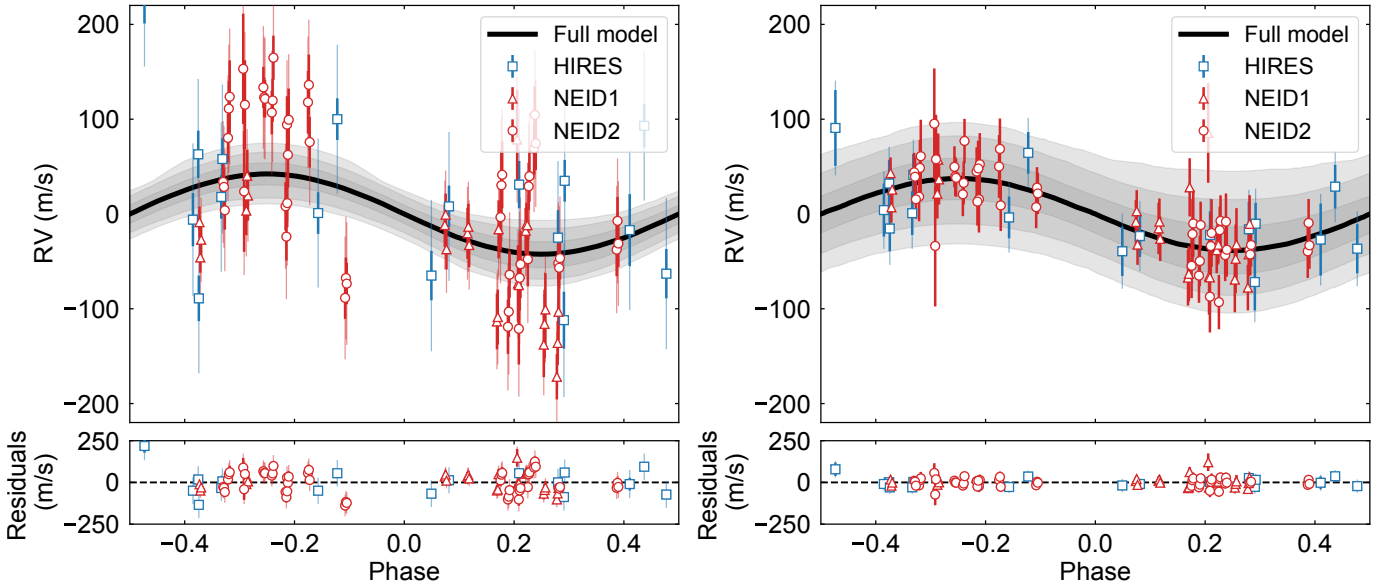

Figure 9. Phased RVs and best-fit model, without a Gaussian process (left) and with a quasi-periodic Gaussian process (right). The data points on the right are detrended by the Gaussian process component of the model, which effectively improves agreement between the data and the model.

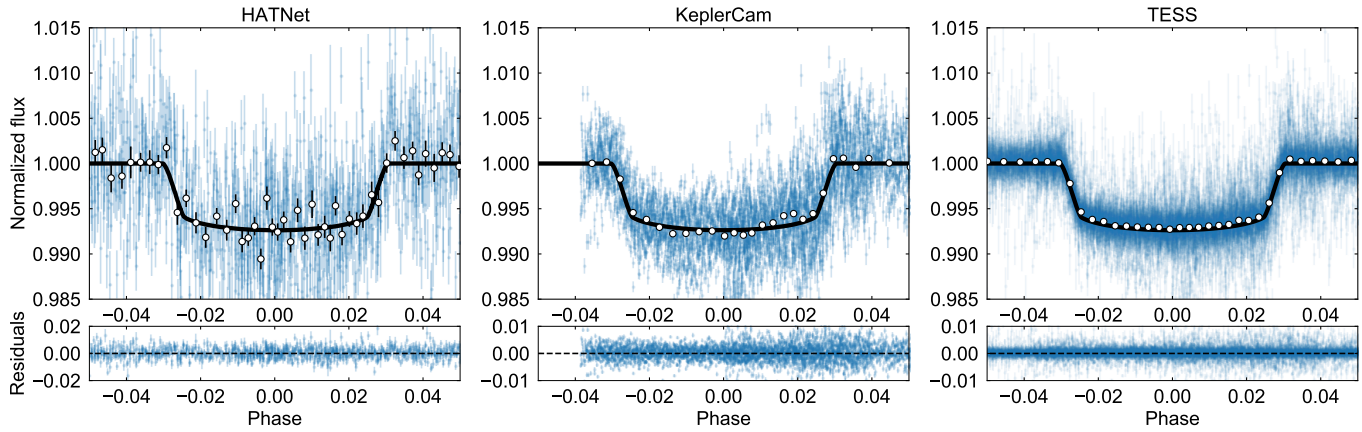

Figure 10. Phased raw (blue) and binned (white circles) photometry data points. Best-fit models (black lines) and residuals are also included.

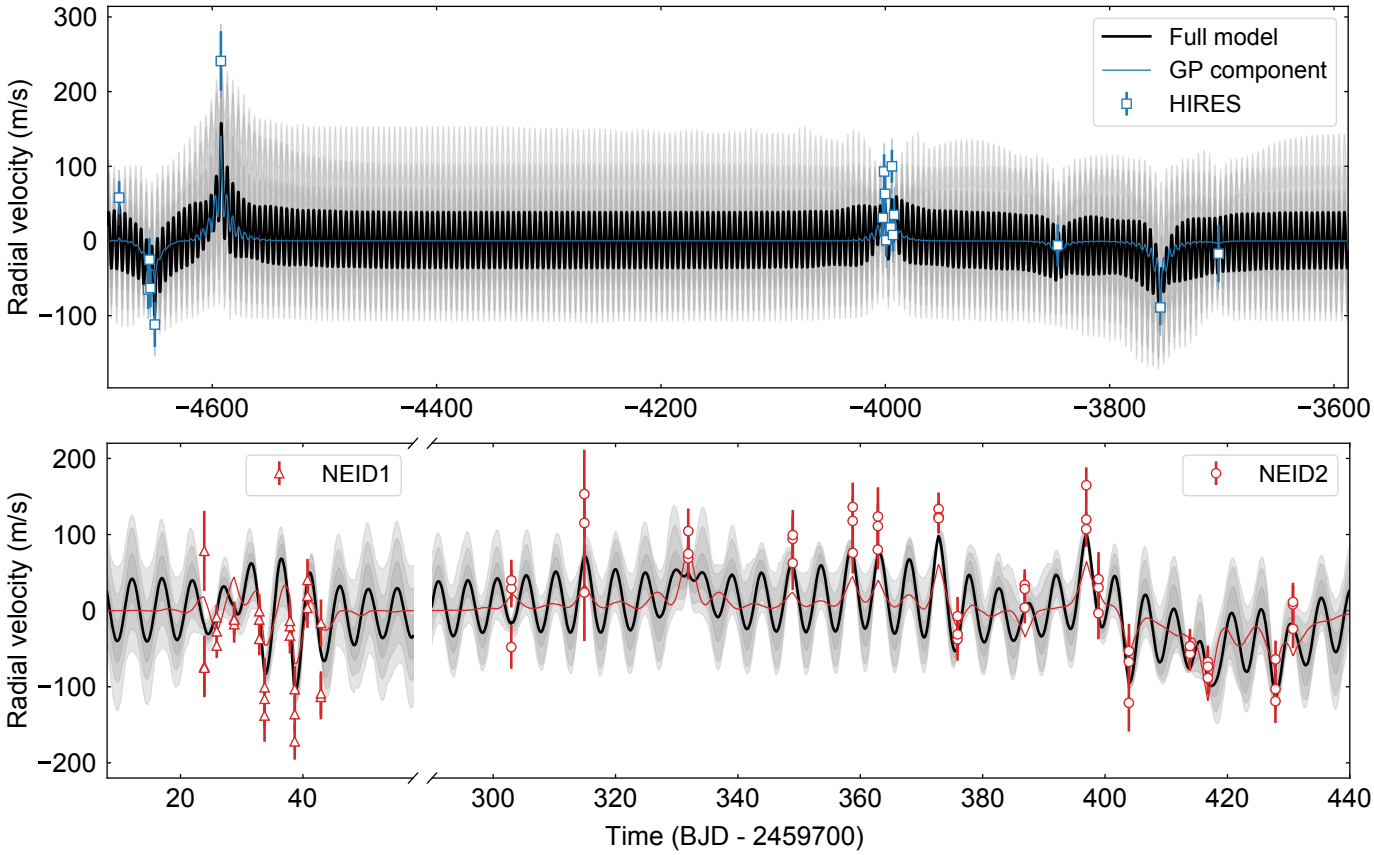

Figure 11. Same as Figure 8, but for the full model which includes a by-instrument quasi-periodic Gaussian process component. The blue and red lines represent the GP component for the HIRES and NEID data respectively.

and detailed atmospheric characterization as suggested by Batalha et al. (2019), which was the initial goal of the NEID observing strategy.

This revised density maintains HAT-P-67 b's position as one of the lowest-density planets known, placing it well outside the boundaries of the mass-radius distribution for known hot giants (see Figure 12). It is the largest known planet, and its nominal density makes it the second least dense transiting planet with $T_{\rm eq} > 1000$ K.

Models from Thorngren et al. (2023) suggest that a hot Saturn in the current location of HAT-P-67 b in mass-radius space will lose the majority of its gaseous

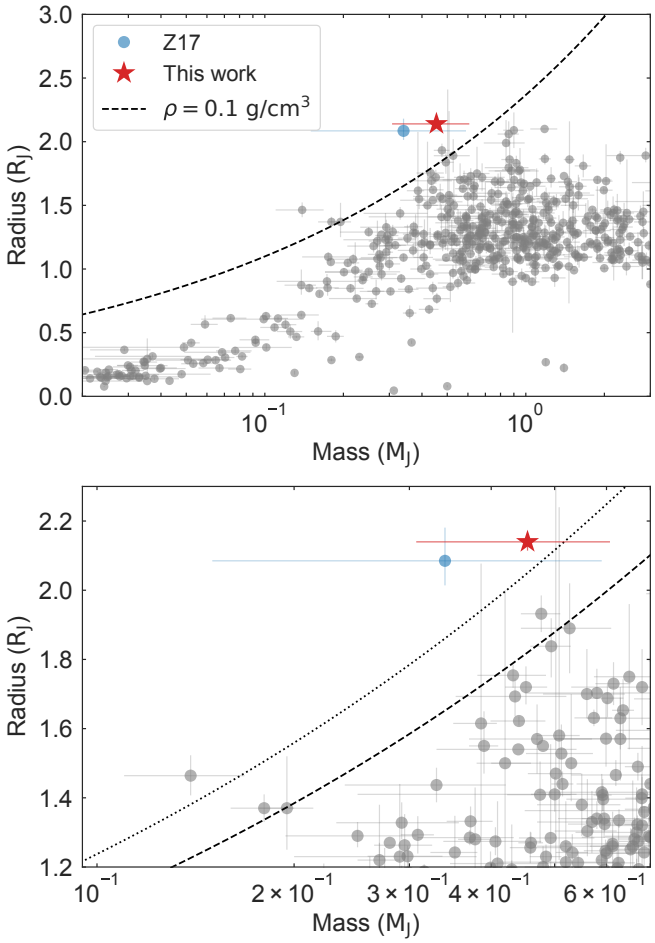

Figure 12. Top: Mass-radius plot of known transiting exoplanets with equilibrium temperatures greater than 1000 K. The original location of HAT-P-67 b from Z17 is marked by a blue shaded circle and the updated location from this work by a red star. HAT-P-67 b is the largest known hot giant planet, and is one of only four planets to cross the $\rho = 0.1$ g cm^{-3} boundary. **Bottom:** Zoomed-in version, with curves representing $\rho = 0.07$ g cm^{-3} and 0.1 g cm^{-3}. The only other planet with $\rho < 0.07$ g cm^{-3} is WASP-193b.

envelope within ~ 0.05 Gyr, after which it will retain only its core of $5 - 15\ M_\oplus$ (Gully-Santiago et al. 2024).

4.2. *Coincidence of Stellar Rotation and Planetary Orbit*

The proximity of the measured stellar rotation period of 5.4 ± 0.1 days to the planet's orbital period of 4.8 days could be coincidental, or due to secular tidal interactions between the star and planet (Gully-Santiago et al. 2024). Alternatively, a more complicated interaction between the planetary magnetic field and the star could cause this coincidence of periods (e.g. Star-Planet Magnetic Interaction, or SPMI, Strugarek 2018). Correlation between stellar activity indicators and the planetary orbital period can be indicative of SPMI, but this correlation is not always present, as changes in the stellar magnetic field can produce periods of stellar rotation correlated activity and orbital period correlated activity (e.g. Shkolnik et al. 2008). The SPMI interpretation is disfavored by Gully-Santiago et al. (2024) because they do not observe significant variability in the Hα and Ca II HK lines. However, our data suggests there is excess periodogram power in the Hα line and stellar photometry, both at the planetary period, which could possibly be an indication of planetary orbit correlated activity.

4.3. *Stellar Evolution*

Due to HAT-P-67's large current radius and its expected further inflation as it continues to evolve off the main sequence, its radius will eventually increase past the orbit of HAT-P-67 b, thus engulfing the planet. To estimate the timescale of such an event, we use MESA 1-D stellar evolutionary models for a star at the mass of HAT-P-67 A (1.73 $M_\odot$). The MESA models are configured following a similar methodology as described in L. Wang & K. Schlaufman (in prep). Using the median stellar parameters derived from our isochrone fit as inputs, we evolve the host star through its evolutionary phases up to the onset of the core helium flash. Additionally, the luminosity of the host star will dramatically increase in the near future, accelerating the planet's evaporation. The modeled luminosity over time is shown in Figure 13.

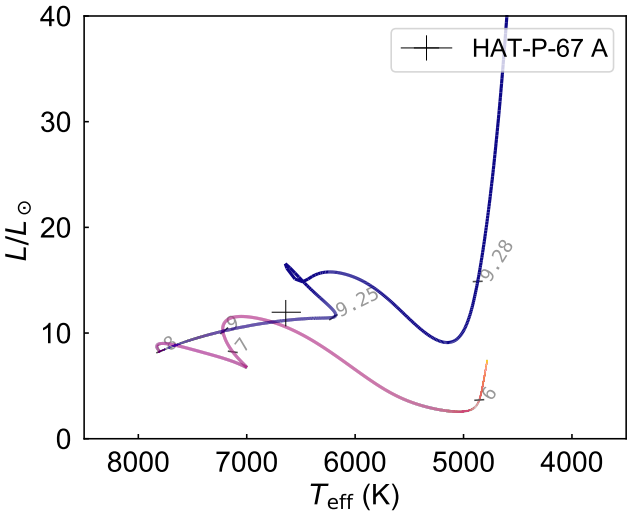

Figure 13. Evolution of a 1.73 $M_\odot$ star from MESA in luminosity-$T_{\rm eff}$ space. The current parameters of HAT-P-67 A are plotted as the black cross, and the gray numbers represent the logarithm of the age of the star in years.

4.4. *Tidal Evolution*

To investigate potential futures of HAT-P-67 b and whether orbital decay may be observable, we integrate the coupled system of ordinary differential equations (ODEs) modeling the tidal evolution process presented in Leconte et al. (2010), following a similar process as Schmidt et al. (2024). This system of ODEs is based on the complete tidal evolution equations of the Hut (1981) model and is valid at any order in eccentricity, obliquity, and spin. We use the MESA stellar track radius and the newly derived planet mass and radius as our planet parameter inputs. We account for the rotation evolution of the host star due to stellar evolution by calculating its current angular momentum with our TESS-derived rotation period. We use the stellar moment of inertia coefficient from a solar-composition, median-rotation $M_* = 1.5\ M_\odot$ stellar model from the Amard et al. (2019) grid. As the star expands, we slow the star's rotation to conserve angular momentum. We assume that the planet is on a circular orbit, that its rotation period is synchronized with its orbital period, that its tidal quality factor $Q_\mathrm{p} = 10^6$, and that its present-day obliquity matches its slight misalignment of 2.2° (Sicilia et al. 2024). We vary the stellar tidal quality factor Q'_* across a plausible range of values for hot Jupiters (Barker 2020; Weinberg et al. 2024). We find $Q'_* \lesssim 10^6$ would result in the planet's tidal disruption in $100 - 200$ Myr, prior to the star's rapid expansion as it evolves off the main sequence, while $Q'_* \gtrsim 10^6$ would result in the planet's engulfment by the star in about 250 Myr, during the star's post-main sequence evolution. We conclude that 250 Myr is an upper bound for the disruption/engulfment timescale. In both scenarios, it is unlikely for any orbital decay to be observable ($|dP/dt| < 1$ ms yr^{-1}) at the present day. We plot the result of this calculation in Figure 14.

5. CONCLUSION

In this work, we present an analysis of the HAT-P-67 b system, making use of existing ground- and space-based photometry in addition to newly acquired RV data. We update the various parameters of HAT-P-67 b to greater precision, and in particular update its mass to be 0.45 ± 0.15 M$_\mathrm{J}$, consistent with previous measurements but with a uncertainty which has been reduced from 75% (Z17) to 33%.

Additionally, our work underscores the impact stellar activity may have on the determination of planet parameters. Through a detailed analysis of the available photometric and spectroscopic data, we find that the rapid rotation of the host star (and potentially SPMI) induces radial velocity signals at timescales comparable to the orbital period of the planet and with amplitudes comparable to the planetary amplitude. We use a physically motivated quasi-periodic Gaussian process to disentangle the stellar activity from the star's barycentric motion, which yields a mass measurement that is consistent with using no Gaussian process but has a more realistic uncertainty that captures the RV variability due to the stellar activity (see §3.5.3).

Our work solidifies HAT-P-67 b as one of the lowest-density transiting planets known to date, as one of only four hot ($T_\mathrm{eq} > 1000$ K) planets with densities below 0.1 g cm^{-3}. Models of runaway mass loss imply that HAT-P-67 b will quickly evaporate on the timescale of ~ 0.05 Gyr (Thorngren et al. 2023), leaving only the planet's core (a few to tens of Earth masses) behind. HAT-P-67 b's unique position in the hot-Saturn population is due to 1) the recent evolution of the host star off the main sequence, which has not had enough time to strip away the planet's atmosphere and engulf its core, and 2) fortuitous timing, allowing us to capture the planet in its current highly inflated state.

HAT-P-67 b's low density, now measured to 33% precision, positions it as a unique target for atmospheric characterization through transmission spectroscopy. There are already multiple existing works in the literature which find a large escaping helium tail and high mass loss rates for this planet (Gully-Santiago et al. 2024; Bello-Arufe et al. 2023; Sicilia et al. 2024), and the bulk parameter constraints that we have placed on HAT-P-67 b will aid in the interpretation of both past and future observations of this intriguing target.

ACKNOWLEDGMENTS

We would like to thank the anonymous reviewer for their feedback, which improved this paper. We would like to thank the firefighters for their bravery and service to the observatory in the face of the Contreras wildfire. We would like to sincerely thank David Ardila, Heidi Schweiker, and the WIYN board and management for their generosity in managing our program in the aftermath of the Contreras wildfire.

This work uses data collected from the WIYN telescope situated on I'oligam Du'ag (Kitt Peak). The authors would like to extend their deepest gratitude to the Tohono O'odham Nation for their stewardship of Kitt Peak and recognize the important cultural significance this mountain holds for the indigenous community. The authors are most fortunate to conduct astronomical observations from this land.

This paper contains data taken with the NEID instrument, which was funded by the NASA-NSF Exoplanet Observational Research (NN-EXPLORE) partnership and built by the Pennsylvania State Univer-

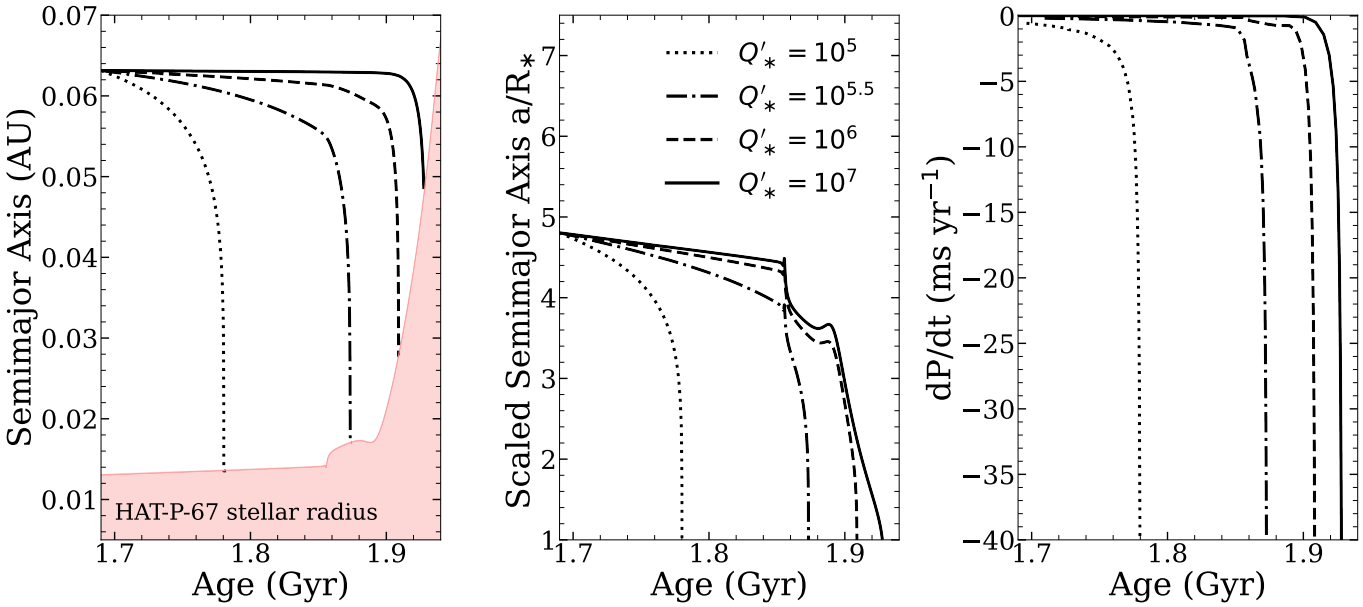

Figure 14. Model for the self-consistent tidal evolution of the HAT-P-67 system. We plot as black lines the semimajor axis (left), scaled semimajor axis a/R_* (center), and orbital decay rate dP/dt (right) as functions of time in Gyr. As the tidal quality factor Q'_* for the host star is unknown, we model four potential cases spanning the plausible range of hot Jupiter host stars (Barker 2020; Weinberg et al. 2024): 10^5 (dotted lines), $10^{5.5}$ (dash-dotted lines), 10^6 (dashed lines), and 10^7 (solid lines). We start the planet at a semimajor axis of 0.06303 AU (corresponding to its present-day period of 4.8 days), assuming $Q_{\rm p} = 10^6$, a circular orbit, synchronized rotation and revolution, and a small nonzero obliquity of 2.2° (Sicilia et al. 2024). We evolve the planet from its current age of 1.69 Gyr to the point it reaches its host star's radius. If HAT-P-67's Q'_* is on the higher end of the typical range, the planet will be engulfed in about 250 Myr; on the other hand, if HAT-P-67's Q'_* is on the lower end of the typical range similar to that of WASP-12 (Yee et al. 2020), then the planet will be tidally disrupted in 100 to 200 Myr, demonstrating HAT-P-67 b to be a doomed world. Regardless of which scenario occurs, this orbital decay is unlikely be detectable for any plausible Q'_* value.

sity. NEID is installed on the WIYN telescope, which is operated by the National Optical Astronomy Observatory, and the NEID archive is operated by the NASA Exoplanet Science Institute at the California Institute of Technology. NN-EXPLORE is managed by the Jet Propulsion Laboratory, California Institute of Technology under contract with the National Aeronautics and Space Administration. This work was supported by a NASA WIYN PI Data Award, administered by the NASA Exoplanet Science Institute.

Data presented in this paper are based on observations obtained with the Hungarian-made Automated Telescope Network at the HAT station at the Submillimeter Array of SAO and the HAT station at the Fred Lawrence Whipple Observatory of SAO.

This work is based on observations obtained with the 1.2 m telescope operated by the Smithsonian Astrophysical Observatory at Fred Lawrence Whipple Observatory in Arizona.

This research has made use of the VizieR catalogue access tool, CDS, Strasbourg, France (DOI: 10.26093/cds/vizier). The original description of the VizieR service was published in Ochsenbein (2000).

This research has made use of the NASA Exoplanet Archive, which is operated by the California Institute of Technology, under contract with the National Aeronautics and Space Administration under the Exoplanet Exploration Program.

This paper includes data collected with the TESS mission, obtained from the MAST data archive at the Space Telescope Science Institute (STScI). The TESS data used in this work can be found at 10.17909/4c8f-f930. Funding for the TESS mission is provided by the NASA Explorer Program. STScI is operated by the Association of Universities for Research in Astronomy, Inc., under NASA contract NAS 5–26555. We acknowledge the use of public TESS data from pipelines at the TESS Science Office and at the TESS Science Processing Operations Center.

This work has made use of data from the European Space Agency (ESA) mission Gaia (https://www.cosmos.esa.int/gaia), processed by the Gaia Data Processing and Analysis Consortium (DPAC, https://www.cosmos.esa.int/web/gaia/dpac/consortium). Funding for the DPAC has been provided by national institu-

tions, in particular the institutions participating in the Gaia Multilateral Agreement.

This publication makes use of data products from the Two Micron All Sky Survey, which is a joint project of the University of Massachusetts and the Infrared Processing and Analysis Center/California Institute of Technology, funded by the National Aeronautics and Space Administration and the National Science Foundation.

This publication makes use of data products from the Wide-field Infrared Survey Explorer, which is a joint project of the University of California, Los Angeles, and the Jet Propulsion Laboratory/California Institute of Technology, funded by the National Aeronautics and Space Administration.

G.W. would like to thank Samuel Grunblatt, Mercedes López-Morales, and Néstor Espinoza for helpful discussions.

Facilities: ADS, CDS, CTIO:2MASS, Exoplanet Archive, FLWO:2MASS, FLWO:1.2m, Gaia, GALEX, HATNet, IRSA, MAST, NEOWISE, TESS, WISE, WIYN

Software: `juliet` (Espinoza et al. 2019a), `astropy` (Astropy Collaboration et al. 2013, 2018, 2022), `dynesty` (Speagle 2020), `isochrones` (Morton 2015), `R` (R Core Team 2024), `matplotlib` (Hunter 2007), `numpy` (Harris et al. 2020), `scipy` (Virtanen et al. 2020), `pandas` (Wes McKinney 2010; pandas development team 2020)

APPENDIX

A. ADDITIONAL TABLES AND PLOTS

Table A1. First 20 lines of activity indicator data from NEID. The full table is available online in machine-readable form.

BJD_{TDB}	dLW	σ_{dLW}	CRX	σ_{CRX}	CaIRT 1	$\sigma_{CaIRT\ 1}$	CaIRT 2	$\sigma_{CaIRT\ 2}$	CaIRT 3	$\sigma_{CaIRT\ 3}$
2459723.87646187	−2563.23	847.30	375.36	380.59	0.6111	0.0056	0.4425	0.0061	0.4793	0.0065
2459723.88356815	−3590.18	651.13	363.27	310.55	0.6144	0.0044	0.4576	0.0046	0.4838	0.0050
2459723.89063798	−2501.34	604.01	−75.14	304.31	0.6069	0.0042	0.4620	0.0044	0.4824	0.0047
2459725.90326585	1683.63	260.33	−198.65	116.69	0.6170	0.0021	0.4547	0.0020	0.4899	0.0022
2459725.91048804	2004.25	255.93	−39.87	105.71	0.6164	0.0020	0.4532	0.0020	0.4877	0.0021
2459725.91775956	2416.96	277.84	−43.98	120.15	0.6163	0.0022	0.4555	0.0021	0.4865	0.0023
2459728.76095795	221.40	387.00	−77.90	179.63	0.6192	0.0028	0.4573	0.0028	0.4905	0.0030
2459728.76826597	255.22	356.06	−217.52	137.09	0.6193	0.0026	0.4587	0.0027	0.4885	0.0028
2459728.77558364	490.23	313.77	34.92	134.28	0.6157	0.0024	0.4563	0.0023	0.4905	0.0025
2459732.86293669	−26.59	370.24	101.85	181.34	0.6145	0.0028	0.4622	0.0028	0.4875	0.0030
2459732.87008587	583.31	354.66	−131.23	158.26	0.6135	0.0027	0.4605	0.0027	0.4894	0.0029
2459732.87739681	31.95	341.16	−176.14	152.08	0.6187	0.0026	0.4610	0.0026	0.4897	0.0027
2459733.72969579	−518.96	551.45	−55.40	246.16	0.6059	0.0039	0.4516	0.0040	0.4923	0.0043
2459733.73686593	−1203.55	579.72	−113.71	252.05	0.6156	0.0042	0.4625	0.0043	0.4850	0.0046
2459733.74416046	−201.61	614.12	572.30	273.96	0.6155	0.0044	0.4612	0.0045	0.4931	0.0048
2459737.87190599	−11.09	431.02	78.88	185.51	0.6128	0.0031	0.4645	0.0031	0.4913	0.0034
2459737.87914954	174.83	387.83	−20.92	172.68	0.6197	0.0028	0.4614	0.0029	0.4897	0.0031
2459737.88617648	576.71	373.17	363.04	149.03	0.6148	0.0028	0.4619	0.0028	0.4854	0.0030
2459738.65439909	0.63	382.38	32.86	163.78	0.6198	0.0027	0.4576	0.0027	0.4888	0.0029
2459738.66170780	−479.77	370.98	−80.75	173.98	0.6194	0.0027	0.4578	0.0027	0.4922	0.0028

Table A2. Continued from Table A1. The full table is available online in machine-readable form.

Hα	$\sigma_{\mathrm{H}\alpha}$	NaD 1	$\sigma_{\mathrm{NaD\ 1}}$	NaD 2	$\sigma_{\mathrm{NaD\ 2}}$	PaD	σ_{PaD}	NaNIR	σ_{NaNIR}	Instrument[a]
0.3885	0.0035	0.6623	0.0054	0.7366	0.0056	0.694	0.069	0.0518	0.0061	NEID1
0.3857	0.0027	0.6643	0.0042	0.7430	0.0044	0.763	0.050	0.0530	0.0048	NEID1
0.3862	0.0025	0.6724	0.0040	0.7357	0.0041	0.710	0.045	0.0500	0.0046	NEID1
0.3876	0.0011	0.6659	0.0019	0.7397	0.0020	0.762	0.018	0.0528	0.0022	NEID1
0.3870	0.0011	0.6686	0.0018	0.7440	0.0019	0.745	0.017	0.0513	0.0022	NEID1
0.3875	0.0012	0.6634	0.0020	0.7387	0.0021	0.745	0.019	0.0539	0.0024	NEID1
0.3889	0.0016	0.6578	0.0026	0.7375	0.0028	0.711	0.026	0.0546	0.0031	NEID1
0.3875	0.0015	0.6605	0.0024	0.7436	0.0026	0.708	0.025	0.0540	0.0029	NEID1
0.3872	0.0013	0.6612	0.0022	0.7456	0.0023	0.735	0.021	0.0509	0.0026	NEID1
0.3875	0.0016	0.6744	0.0026	0.7316	0.0027	0.700	0.026	0.0509	0.0030	NEID1
0.3888	0.0015	0.6682	0.0025	0.7364	0.0026	0.724	0.024	0.0469	0.0029	NEID1
0.3870	0.0014	0.6717	0.0024	0.7354	0.0025	0.719	0.022	0.0478	0.0028	NEID1
0.3887	0.0023	0.6705	0.0037	0.7471	0.0038	0.745	0.042	0.0563	0.0042	NEID1
0.3888	0.0024	0.6707	0.0038	0.7394	0.0040	0.814	0.045	0.0498	0.0044	NEID1
0.3912	0.0026	0.6589	0.0040	0.7432	0.0042	0.668	0.046	0.0532	0.0046	NEID1
0.3876	0.0018	0.6630	0.0029	0.7488	0.0031	0.740	0.031	0.0430	0.0034	NEID1
0.3893	0.0016	0.6637	0.0026	0.7512	0.0028	0.745	0.028	0.0412	0.0031	NEID1
0.3882	0.0015	0.6651	0.0026	0.7476	0.0027	0.738	0.027	0.0432	0.0030	NEID1
0.3913	0.0015	0.6600	0.0026	0.7467	0.0027	0.666	0.024	0.0406	0.0030	NEID1
0.3910	0.0015	0.6598	0.0025	0.7470	0.0027	0.704	0.024	0.0468	0.0029	NEID1

[a] NEID1 refers to data collected before the June 2022 Contreras Fire; NEID2 refers to data collected after

REFERENCES

Amard, L., Palacios, A., Charbonnel, C., et al. 2019, A&A, 631, A77, doi: 10.1051/0004-6361/201935160

Arenou, F., Luri, X., Babusiaux, C., et al. 2018, A&A, 616, A17, doi: 10.1051/0004-6361/201833234

Astropy Collaboration, Robitaille, T. P., Tollerud, E. J., et al. 2013, A&A, 558, A33, doi: 10.1051/0004-6361/201322068

Astropy Collaboration, Price-Whelan, A. M., Sipőcz, B. M., et al. 2018, AJ, 156, 123, doi: 10.3847/1538-3881/aabc4f

Astropy Collaboration, Price-Whelan, A. M., Lim, P. L., et al. 2022, ApJ, 935, 167, doi: 10.3847/1538-4357/ac7c74

Bailer-Jones, C. A. L., Rybizki, J., Fouesneau, M., Demleitner, M., & Andrae, R. 2021, AJ, 161, 147, doi: 10.3847/1538-3881/abd806

Bakos, G., Noyes, R. W., Kovács, G., et al. 2004, PASP, 116, 266, doi: 10.1086/382735

Barkaoui, K., Pozuelos, F. J., Hellier, C., et al. 2024, Nature Astronomy, 8, 909, doi: 10.1038/s41550-024-02259-y

Barker, A. J. 2020, MNRAS, 498, 2270, doi: 10.1093/mnras/staa2405

Batalha, N. E., Lewis, T., Fortney, J. J., et al. 2019, ApJL, 885, L25, doi: 10.3847/2041-8213/ab4909

Bello-Arufe, A., Knutson, H. A., Mendonça, J. M., et al. 2023, AJ, 166, 69, doi: 10.3847/1538-3881/acd935

Bianchi, L., Shiao, B., & Thilker, D. 2017, ApJS, 230, 24, doi: 10.3847/1538-4365/aa7053

Blunt, S., Carvalho, A., David, T. J., et al. 2023, AJ, 166, 62, doi: 10.3847/1538-3881/acde78

Busso, G., Cacciari, C., Carrasco, J. M., et al. 2018, Gaia DR2 documentation Chapter 5: Photometry

Casagrande, L., Schönrich, R., Asplund, M., et al. 2011, A&A, 530, A138, doi: 10.1051/0004-6361/201016276

Chabrier, G. 2003, PASP, 115, 763, doi: 10.1086/376392

Choi, J., Dotter, A., Conroy, C., et al. 2016, ApJ, 823, 102, doi: 10.3847/0004-637X/823/2/102

Daylan, T., Günther, M. N., Mikal-Evans, T., et al. 2021, AJ, 161, 131, doi: 10.3847/1538-3881/abd8d2

Dobbs-Dixon, I., Lin, D. N. C., & Mardling, R. A. 2004, ApJ, 610, 464, doi: 10.1086/421510

Dotter, A. 2016, ApJS, 222, 8, doi: 10.3847/0067-0049/222/1/8

Efron, B., Hastie, T., Johnstone, I., & Tibshirani, R. 2004, The Annals of Statistics, 32, 407, doi: 10.1214/009053604000000067

Eisenhardt, P. R. M., Marocco, F., Fowler, J. W., et al. 2020, ApJS, 247, 69, doi: 10.3847/1538-4365/ab7f2a

Espinoza, N., Kossakowski, D., & Brahm, R. 2019a, MNRAS, 490, 2262, doi: 10.1093/mnras/stz2688

Espinoza, N., Brahm, R., Henning, T., et al. 2019b, MNRAS, 491, 2982, doi: 10.1093/mnras/stz3150

Espinoza, N., Pallé, E., Kemmer, J., et al. 2022, AJ, 163, 133, doi: 10.3847/1538-3881/ac4af0

Evans, D. W., Riello, M., De Angeli, F., et al. 2018, A&A, 616, A4, doi: 10.1051/0004-6361/201832756

Fabricius, C., Luri, X., Arenou, F., et al. 2021, A&A, 649, A5, doi: 10.1051/0004-6361/202039834

Feroz, F., & Hobson, M. P. 2008, MNRAS, 384, 449, doi: 10.1111/j.1365-2966.2007.12353.x

Feroz, F., Hobson, M. P., & Bridges, M. 2009, MNRAS, 398, 1601, doi: 10.1111/j.1365-2966.2009.14548.x

Feroz, F., Hobson, M. P., Cameron, E., & Pettitt, A. N. 2019, The Open Journal of Astrophysics, 2, 10, doi: 10.21105/astro.1306.2144

Foreman-Mackey, D., Agol, E., Ambikasaran, S., & Angus, R. 2017, AJ, 154, 220, doi: 10.3847/1538-3881/aa9332

Gaia Collaboration, Brown, A. G. A., Vallenari, A., et al. 2021, A&A, 649, A1, doi: 10.1051/0004-6361/202039657

Gaia Collaboration, Prusti, T., de Bruijne, J. H. J., et al. 2016, A&A, 595, A1, doi: 10.1051/0004-6361/201629272

Gaia Collaboration, Brown, A. G. A., Vallenari, A., et al. 2018, A&A, 616, A1, doi: 10.1051/0004-6361/201833051

Gan, T., Wang, S. X., Teske, J. K., et al. 2020, MNRAS, 501, 6042, doi: 10.1093/mnras/staa3886

Gibson, S. R., Howard, A. W., Marcy, G. W., et al. 2016, Ground-based and Airborne Instrumentation for Astronomy VI, 9908, 990870, doi: 10.1117/12.2233334

Gully-Santiago, M., Morley, C. V., Luna, J., et al. 2024, AJ, 167, 142, doi: 10.3847/1538-3881/ad1ee8

Gupta, A. F., Wright, J. T., Robertson, P., et al. 2021, AJ, 161, 130, doi: 10.3847/1538-3881/abd79e

Hara, N. C., Boué, G., Laskar, J., & Correia, A. C. M. 2016, MNRAS, 464, 1220, doi: 10.1093/mnras/stw2261

Harris, C. R., Millman, K. J., van der Walt, S. J., et al. 2020, Nature, 585, 357, doi: 10.1038/s41586-020-2649-2

Høg, E., Fabricius, C., Makarov, V. V., et al. 2000, A&A, 355, L27

Hunter, J. D. 2007, Computing in Science and Engineering, 9, 90, doi: 10.1109/MCSE.2007.55

Hut, P. 1981, A&A, 99, 126

Jermyn, A. S., Bauer, E. B., Schwab, J., et al. 2023, ApJS, 265, 15, doi: 10.3847/1538-4365/acae8d

Lallement, R., Vergely, J. L., Babusiaux, C., & Cox, N. L. J. 2022, A&A, 661, A147, doi: 10.1051/0004-6361/202142846

Leconte, J., Chabrier, G., Baraffe, I., & Levrard, B. 2010, A&A, 516, A64, doi: 10.1051/0004-6361/201014337

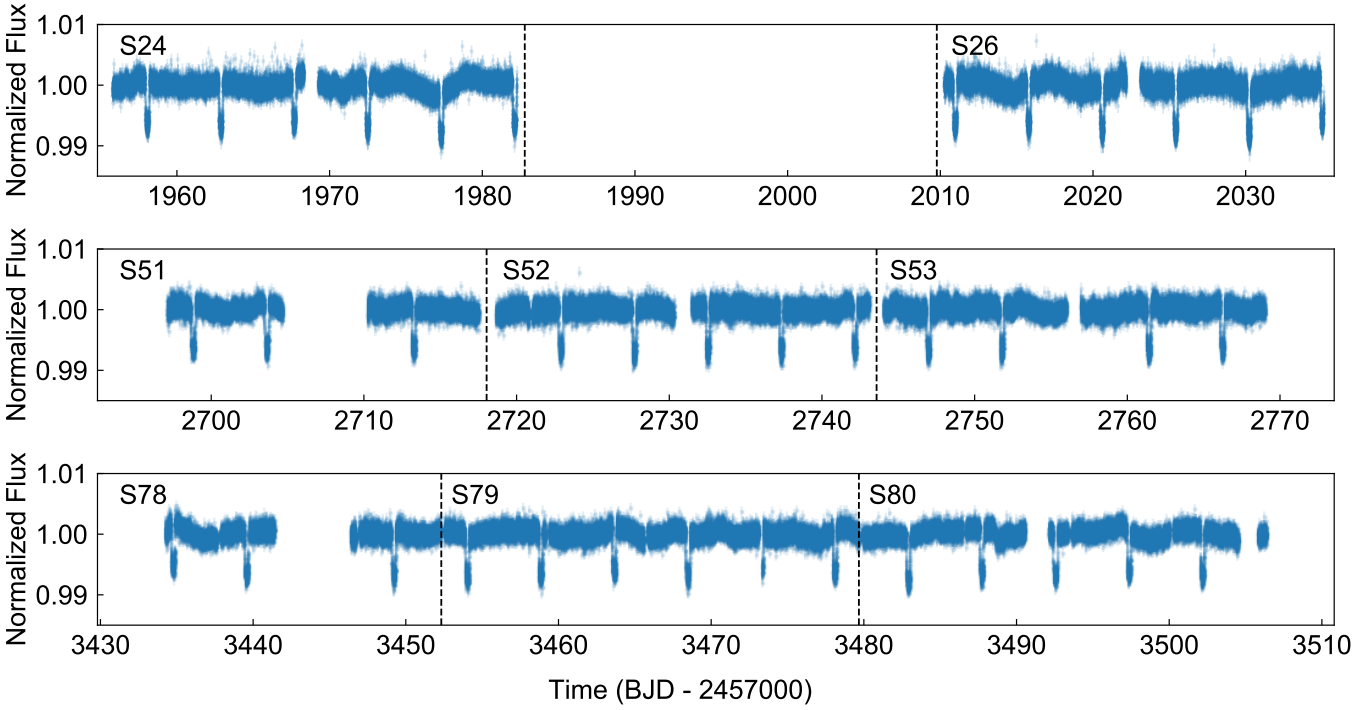

Figure A1. Full light curves from TESS. Data from Years 2, 4, and 6 of the TESS mission are shown in the top, middle, and bottom rows respectively. The data visually suggest a stellar rotation period of a few days. Stellar activity is strongest in Year 2, weakens for Year 4, and returns to elevated levels in Year 6, demonstrating starspots+rotation as a probable cause of the variations.

Lindegren, L., Bastian, U., Biermann, M., et al. 2021a, A&A, 649, A4, doi: 10.1051/0004-6361/202039653

Lindegren, L., Klioner, S. A., Hernández, J., et al. 2021b, A&A, 649, A2, doi: 10.1051/0004-6361/202039709

Lomb, N. R. 1976, Astrophysics and Space Science, 39, 447, doi: 10.1007/BF00648343

Lovis, C., & Fischer, D. 2010, Radial Velocity Techniques for Exoplanets (University of Arizona Press), 27–53

Mahadevan, S., Ramsey, L., Bender, C., et al. 2012, Ground-based and Airborne Instrumentation for Astronomy IV, 8446, 84461S, doi: 10.1117/12.926102

Mainzer, A., Bauer, J., Grav, T., et al. 2011, ApJ, 731, 53, doi: 10.1088/0004-637X/731/1/53

Maíz-Apellániz, J. 2005, PASP, 117, 615, doi: 10.1086/430370

Marocco, F., Eisenhardt, P. R. M., Fowler, J. W., et al. 2021, ApJS, 253, 8, doi: 10.3847/1538-4365/abd805

Mayor, M., & Queloz, D. 1995, Nature, 378, 355, doi: 10.1038/378355a0

McLaughlin, D. B. 1924, ApJ, 60, 22, doi: 10.1086/142826

Morton, T. D. 2015, isochrones: Stellar model grid package, Astrophysics Source Code Library. http://ascl.net/1503.010

Mugrauer, M. 2019, MNRAS, 490, 5088, doi: 10.1093/mnras/stz2673

Nava, C., López-Morales, M., Haywood, R. D., & Giles, H. A. C. 2019, AJ, 159, 23, doi: 10.3847/1538-3881/ab53ec

Nicholson, B. A., & Aigrain, S. 2022, MNRAS, 515, 5251, doi: 10.1093/mnras/stac2097

Ochsenbein, F. 2000, The VizieR database of astronomical catalogues, doi: 10.26093/cds/vizier

pandas development team, T. 2020, pandas-dev/pandas: Pandas, latest, Zenodo, doi: 10.5281/zenodo.3509134

Paxton, B., Bildsten, L., Dotter, A., et al. 2011, ApJS, 192, 3, doi: 10.1088/0067-0049/192/1/3

Paxton, B., Cantiello, M., Arras, P., et al. 2013, ApJS, 208, 4, doi: 10.1088/0067-0049/208/1/4

Paxton, B., Schwab, J., Bauer, E. B., et al. 2018, ApJS, 234, 34, doi: 10.3847/1538-4365/aaa5a8

Paxton, B., Smolec, R., Schwab, J., et al. 2019, ApJS, 243, 10, doi: 10.3847/1538-4365/ab2241

Pepe, F., Cristiani, S., Rebolo, R., et al. 2021, A&A, 645, A96, doi: 10.1051/0004-6361/202038306

Perryman, M. 2018, The exoplanet handbook (Cambridge university press)

R Core Team. 2024, R: A Language and Environment for Statistical Computing, R Foundation for Statistical Computing, Vienna, Austria. https://www.R-project.org/

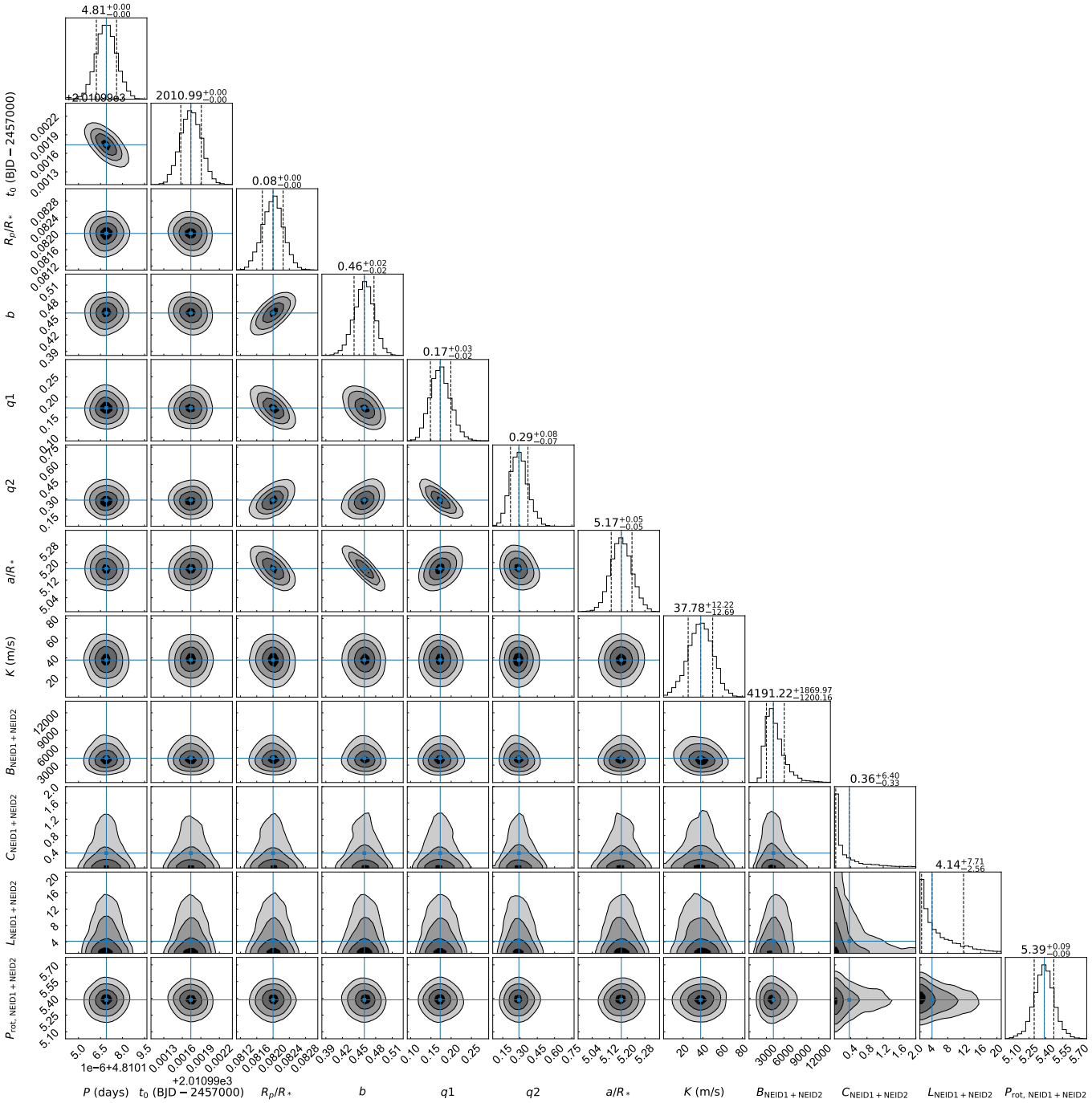

Figure A2. Corner plot for joint (photometry+RVs) fit which includes one planet and a quasi-periodic GP. We adopt this fit as final. We include only the planetary parameters and GP parameters for the NEID data for clarity.

Ricker, G. R., Winn, J. N., Vanderspek, R., et al. 2014, Journal of Astronomical Telescopes, Instruments, and Systems, 1, 014003, doi: 10.1117/1.JATIS.1.1.014003

Riello, M., De Angeli, F., Evans, D. W., et al. 2018, A&A, 616, A3, doi: 10.1051/0004-6361/201832712

Robertson, P., Roy, A., & Mahadevan, S. 2015, ApJL, 805, L22, doi: 10.1088/2041-8205/805/2/L22

Robertson, P., Anderson, T., Stefansson, G., et al. 2019, Journal of Astronomical Telescopes, Instruments, and Systems, 5, 015003, doi: 10.1117/1.JATIS.5.1.015003

Rossiter, R. A. 1924, ApJ, 60, 15, doi: 10.1086/142825

Rowell, N., Davidson, M., Lindegren, L., et al. 2021, A&A, 649, A11, doi: 10.1051/0004-6361/202039448

Saar, S. H., & Donahue, R. A. 1997, ApJ, 485, 319, doi: 10.1086/304392

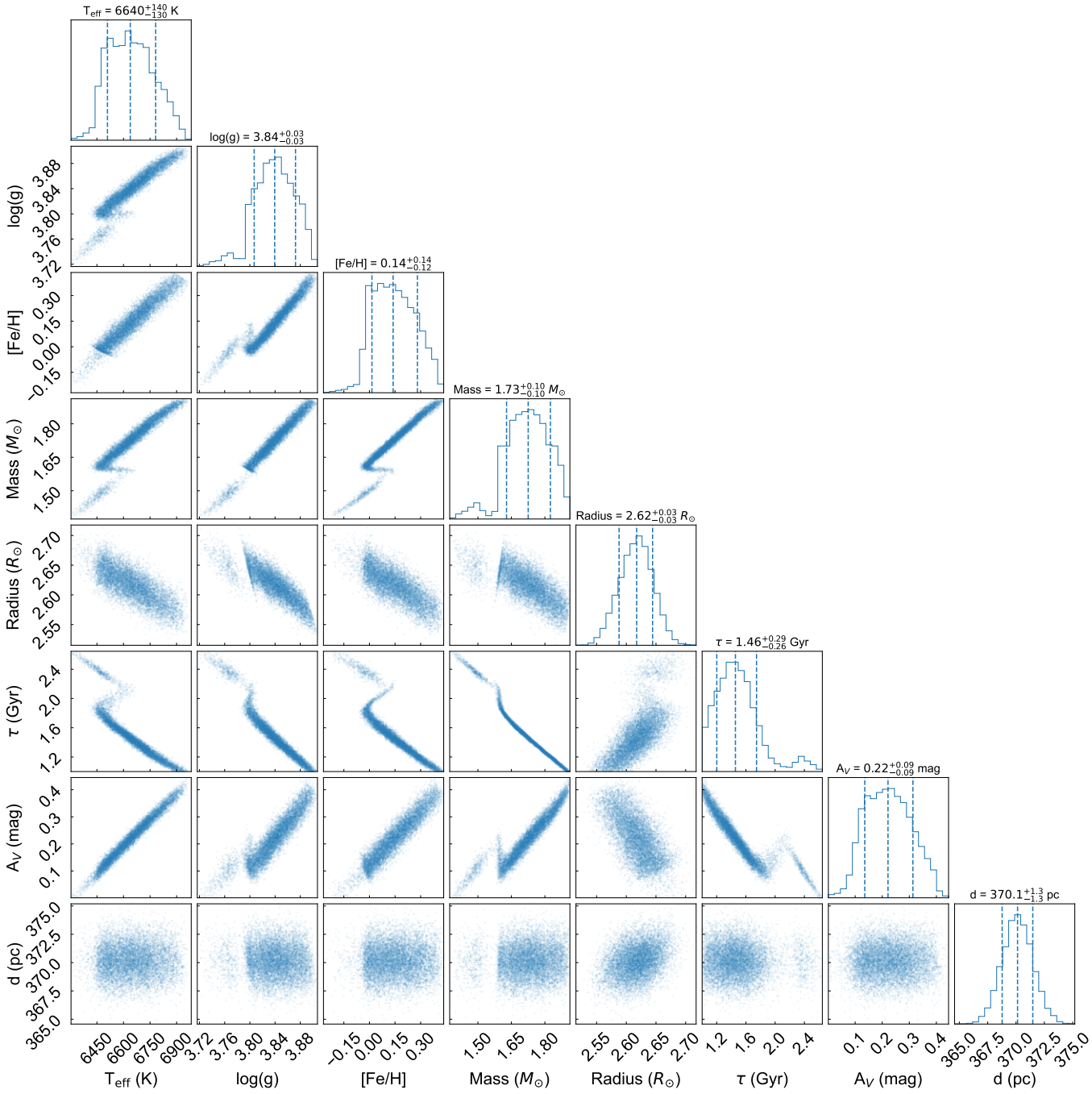

Figure A3. Corner plot for HAT-P-67A fit.

Salpeter, E. E. 1955, ApJ, 121, 161, doi: 10.1086/145971

Scargle, J. D. 1982, ApJ, 263, 835, doi: 10.1086/160554

Schmidt, S. P., Schlaufman, K. C., & Hamer, J. H. 2024, AJ, 168, 109, doi: 10.3847/1538-3881/ad5d76

Schwab, C., Rakich, A., Gong, Q., et al. 2016, Ground-based and Airborne Instrumentation for Astronomy VI, 9908, 99087H, doi: 10.1117/12.2234411

Shkolnik, E., Bohlender, D. A., Walker, G. A. H., & Collier Cameron, A. 2008, ApJ, 676, 628, doi: 10.1086/527351

Sicilia, D., Scandariato, G., Guilluy, G., et al. 2024, A&A, 687, A143, doi: 10.1051/0004-6361/202349116

Skrutskie, M. F., Cutri, R. M., Stiening, R., et al. 2006, AJ, 131, 1163, doi: 10.1086/498708

Speagle, J. S. 2020, MNRAS, 493, 3132, doi: 10.1093/mnras/staa278

Stefansson, G., Hearty, F., Robertson, P., et al. 2016, ApJ, 833, 175, doi: 10.3847/1538-4357/833/2/175

Stefànsson, G., Mahadevan, S., Petrovich, C., et al. 2022, ApJL, 931, L15, doi: 10.3847/2041-8213/ac6e3c

Strugarek, A. 2018, in Handbook of Exoplanets, ed. H. J. Deeg & J. A. Belmonte (Springer), 25, doi: 10.1007/978-3-319-55333-7_25

Struve, O. 1952, The Observatory, 72, 199

Suárez Mascareño, A., Damasso, M., Lodieu, N., et al. 2022, Nature Astronomy, 6, 232, doi: 10.1038/s41550-021-01533-7

Thorngren, D. P., Lee, E. J., & Lopez, E. D. 2023, ApJL, 945, L36, doi: 10.3847/2041-8213/acbd35

Torra, F., Castañeda, J., Fabricius, C., et al. 2021, A&A, 649, A10, doi: 10.1051/0004-6361/202039637

Tran, Q. H., & Bowler, B. P. 2024, AJ, 168, 183, doi: 10.3847/1538-3881/ad698b

van Saders, J. L., & Pinsonneault, M. H. 2013, ApJ, 776, 67, doi: 10.1088/0004-637X/776/2/67

Vergely, J. L., Lallement, R., & Cox, N. L. J. 2022, A&A, 664, A174, doi: 10.1051/0004-6361/202243319

Virtanen, P., Gommers, R., Oliphant, T. E., et al. 2020, Nature Methods, 17, 261, doi: 10.1038/s41592-019-0686-2

Vogt, S. S., Allen, S. L., Bigelow, B. C., et al. 1994, 2198, 362, doi: 10.1117/12.176725

Weinberg, N. N., Davachi, N., Essick, R., et al. 2024, ApJ, 960, 50, doi: 10.3847/1538-4357/ad05c9

Wes McKinney. 2010, 56, doi: 10.25080/Majora-92bf1922-00a

Wright, E. L., Eisenhardt, P. R. M., Mainzer, A. K., et al. 2010, AJ, 140, 1868, doi: 10.1088/0004-6256/140/6/1868

Yee, S. W., Winn, J. N., Knutson, H. A., et al. 2020, ApJ, 888, L5, doi: 10.3847/2041-8213/ab5c16

Zechmeister, M., Reiners, A., Amado, P. J., et al. 2018, A&A, 609, A12, doi: 10.1051/0004-6361/201731483

Zhou, G., Bakos, G. Á., Hartman, J. D., et al. 2017, AJ, 153, 211, doi: 10.3847/1538-3881/aa674a